Universiteit
Leiden
The Netherlands

The MAGPI survey: effects of spiral arms on different tracers of the interstellar medium and stellar populations at z ~ 0.3

Chen, Q.H.; Grasha, K.; Battisti, A.J.; Wisnioski, E.; Mendel, T.; Sharda, P.; ... ; Kewley, L.

Citation
Chen, Q. H., Grasha, K., Battisti, A. J., Wisnioski, E., Mendel, T., Sharda, P., … Kewley, L. (2023). The MAGPI survey: effects of spiral arms on different tracers of the interstellar medium and stellar populations at z ~ 0.3. *Monthly Notices Of The Royal Astronomical Society, 527*(2), 2991-3005. doi:10.1093/mnras/stad3348

Version:	Publisher's Version
License:	Creative Commons CC BY 4.0 license
Downloaded from:	https://hdl.handle.net/1887/4308011

Note: To cite this publication please use the final published version (if applicable).

The MAGPI survey: effects of spiral arms on different tracers of the interstellar medium and stellar populations at $z \sim 0.3$

Qian-Hui Chen (陈千惠), Kathryn Grasha, Andrew J Battisti, Emily Wisnioski, Trevor Mendel, Piyush Sharda, Giulia Santucci, Zefeng Li (李泽峰), Caroline Foster, Marcie Mun, Hye-Jin Park, Takafumi Tsukui, Gauri Sharma, Claudia D P Lagos, Stefania Barsanti, Lucas M Valenzuela, Anshu Gupta, Sabine Thater, Yifei Jin (金刈非), Lisa Kewley

Downloaded from https://academic.oup.com/mnras/article/527/2/2991/7339769 by guest on 22 July 2026

Monthly Notices of the ROYAL ASTRONOMICAL SOCIETY

MNRAS **527,** 2991–3005 (2024) https://doi.org/10.1093/mnras/stad3348
Advance Access publication 2023 November 3

The MAGPI survey: effects of spiral arms on different tracers of the interstellar medium and stellar populations at $z \sim 0.3$

Qian-Hui Chen (陈千惠)[1,2★] Kathryn Grasha[1,2,3†] Andrew J. Battisti[1,2] Emily Wisnioski[1,2] Trevor Mendel,[1,2] Piyush Sharda[4] Giulia Santucci[2,5] Zefeng Li (李泽峰)[1,2] Caroline Foster[2,6] Marcie Mun,[1,2] Hye-Jin Park,[1,2] Takafumi Tsukui[1,2] Gauri Sharma,[7,8] Claudia D. P. Lagos,[5,9] Stefania Barsanti[1,2,10] Lucas M. Valenzuela[11] Anshu Gupta,[2,12] Sabine Thater,[13] Yifei Jin (金闪非)[1,2,14] and Lisa Kewley[1,2,14]

[1]*Research School of Astronomy and Astrophysics, Australian National University, Canberra, ACT 2611, Australia*
[2]*ARC Centre of Excellence for All Sky Astrophysics in 3 Dimensions (ASTRO 3D), Stromlo, ACT 2611, Australia*
[3]*Harvard-Smithsonian Center for Astrophysics, 60 Garden Street, Cambridge, MA 02138, USA*
[4]*Leiden Observatory, Leiden University, PO Box 9513, NL-2300 RA Leiden, the Netherlands*
[5]*International Centre for Radio Astronomy Research, The University of Western Australia, 35 Stirling Highway, Crawley, WA 6009, Australia*
[6]*School of Physics, University of New South Wales, Sydney, NSW 2052, Australia*
[7]*University of Western Cape, Bellville, Cape Town 7535, South Africa*
[8]*INFN – Sezione di Trieste, via Valerio 2, I-34127 Trieste, Italy*
[9]*Cosmic Dawn Center (DAWN), University of Copenhagen, DK-1172 Copenhagen, Denmark*
[10]*Sydney Institute for Astronomy (SIfA), School of Physics, The University of Sydney, Sydney, NSW 2006, Australia*
[11]*Fakultät für Physik, Ludwig-Maximilians-Universität München, Universitäts-Sternwarte, Scheinerstraße 1, D-81679 München, Germany*
[12]*International Centre for Radio Astronomy Research (ICRAR), Curtin University, Bentley, WA 6102, Australia*
[13]*Department of Astrophysics, University of Vienna, Türkenschanzstraße 17, A-1180 Vienna, Austria*
[14]*Institute for Theory and Computation, Harvard-Smithsonian Center for Astrophysics, Cambridge, MA 02138, USA*

Accepted 2023 October 30. Received 2023 October 29; in original form 2023 June 22

ABSTRACT

Spiral structures are important drivers of the secular evolution of disc galaxies, however, the origin of spiral arms and their effects on the development of galaxies remain mysterious. In this work, we present two three-armed spiral galaxies at $z \sim 0.3$ in the Middle Age Galaxy Properties with Integral Field Spectroscopy (MAGPI) survey. Taking advantage of the high spatial resolution (∼0.6 arcsec) of the Multi-Unit Spectroscopic Explorer (MUSE), we investigate the two-dimensional (2D) distributions of different spectral parameters: Hα, gas-phase metallicity, and D_{4000}. We notice significant offsets in Hα (∼0.2 dex) and gas-phase metallicities (∼0.05 dex) among the spiral arms, downstream and upstream of MAGPI 1202197197 (SG 1202). This observational signature suggests the spiral structure in SG 1202 is consistent with arising from density wave theory. No azimuthal variation in Hα or gas-phase metallicities is observed in MAGPI 1204198199 (SG 1204), which can be attributed to the tighter spiral arms in SG 1204 than SG 1202, coming with stronger mixing effects in the disc. The absence of azimuthal D_{4000} variation in both galaxies suggests the stars at different ages are well mixed between the spiral arms and distributed around the disc regions. The different azimuthal distributions in Hα and D_{4000} highlight the importance of time-scales traced by various spectral parameters when studying 2D distributions in spiral galaxies. This work demonstrates the feasibility of constraining spiral structures by tracing interstellar medium (ISM) and stellar population at $z \sim 0.3$, with a plan to expand the study to the full MAGPI survey.

Key words: ISM: evolution – galaxies: abundances – galaxies: evolution – galaxies: ISM – galaxies: spiral.

1 INTRODUCTION

In the local Universe, the majority of star formation takes place in spiral galaxies (Brinchmann et al. 2004) and up to two-thirds of all massive galaxies are spiral galaxies (Lintott et al. 2011; Willett et al. 2013). The interplay between star formation activity and the influence of spiral structures is closely related to (1) the physical conditions and distribution of the gas in the interstellar medium (ISM), and (2) the processes by which stars are created from the molecular gas. Spiral structures are complex and diverse, which is demonstrated by the variety in their number of arms, pitch angles, amplitudes, and longevity (Dobbs & Baba 2014). Despite their ubiquitous nature, we

★ E-mail: qianhui.chen@anu.edu.au
† ARC DECRA Fellow.

© The Author(s) 2023.
Published by Oxford University Press on behalf of Royal Astronomical Society. This is an Open Access article distributed under the terms of the Creative Commons Attribution License (http://creativecommons.org/licenses/by/4.0/), which permits unrestricted reuse, distribution, and reproduction in any medium, provided the original work is properly cited.

Downloaded from https://academic.oup.com/mnras/article/527/2/2991/7339769 by guest on 22 July 2026

know surprisingly little of the physical origin of spiral features and how they evolve over cosmic time (Sellwood & Masters 2022).

Previous studies investigating spiral-driven evolution have revealed the physical complexities of the origin of spiral features, including self-excited instabilities in equilibrium discs and gravitational instabilities due to interactions with companions, haloes, and stellar bars. We summarize the two main physical mechanisms for the origin of spiral arms in disc galaxies.

(i) (Quasi-stationary) density wave theory (Lin & Shu 1966). Spiral arms are density waves that evolve slowly and rotate at a fixed angular velocity (i.e. pattern speed) across the galaxy. The stars and gas in the disc orbit at different angular velocities, depending on their distances to the galaxy centre, which is called differential rotation. The corotation radius is the radius where the angular velocity of the material matches the pattern speed (e.g. Pour-Imani et al. 2016; Peterken et al. 2019). In this theory, the material is left behind the density wave outside the corotation radius but overtakes the density wave while inside the corotation radius. When entering the spiral potential, the gas will collapse (Toomre 1977) and undergo shocks (Roberts 1970; Bonnell et al. 2006), which are observable as periodic episodes of intense and instantaneous star formation (Aouad, James & Chilingarian 2020). The formation of a global spiral pattern from the density wave theory is caused by an instability of the disc as a direct result of self-gravity (Pettitt et al. 2017). According to the density wave theory, spiral galaxies with more than three spiral arms are less stable compared to grand-design spiral galaxies with two arms (Thomasson et al. 1990). Simulations report long-lived grand-design spiral galaxies that resemble the density wave theory, although the overall spiral pattern is transient and recurrent (Sellwood 2011; D'Onghia, Vogelsberger & Hernquist 2013; Sellwood & Carlberg 2014). The maintenance (or the necessity of maintenance) of long-lived spiral waves is still an open question.

(ii) Dynamic spirals (Sellwood & Carlberg 1984; Fuchs 2001; Dobbs & Baba 2014). In the dynamic material wave model, a leading density pattern transfers into a trailing one due to the shear caused by a differentially rotating disc. During the rotation, the leading mode is amplified into a spiral arm as a result of the self-gravity, through a mechanism called swing amplification (Goldreich & Lynden-Bell 1965). In this mechanism, spiral arms are simply a superposition of many unstable waves (Michikoshi & Kokubo 2016). There is no specific pattern speed for dynamic spirals or significant offset between the rotation of spirals and the disc. Thus, gas does not pass through the spiral arms but instead falls into the minimal potential from both sides of the arms (Dobbs & Bonnell 2008; Wada, Baba & Saitoh 2011). The spirals generated by swing amplification are transient, recurrent, and short-lived (Sellwood & Carlberg 2014, 2019). Swing amplification typically assembles flocculent or multi-armed galaxies but is capable of generating grand-design spiral arms (Baba 2015). Sellwood & Carlberg (1984) argue for short-lived (a few $\sim$100 Myr) dynamic spirals due to the heating from dissipation. On the other hand, Fujii et al. (2011) and D'Onghia, Vogelsberger & Hernquist (2013) demonstrate the possibility of long-lasting (up to $\sim$10 Gyr) dynamic spirals using highly spatially resolved *N*-body simulations.

The density wave theory and dynamic spiral theory are not exclusive to each other. Instead, the two mechanisms can explain the origin and assembly of different spiral arms. Many studies have been conducted to investigate the feasibility of these two theories through simulations. Since the 1970s, transitory spiral features have been seen in some simulations (Miller, Prendergast & Quirk 1970; Hohl 1971; Hockney & Brownrigg 1974), which give us a glimpse of the fundamental physics of spirals. Assuming different models of spirals, simulations test, and improve the theories by revealing the longevity of spiral arms (Oh et al. 2008; Fujii et al. 2011; Struck, Dobbs & Hwang 2011; D'Onghia, Vogelsberger & Hernquist 2013; Sellwood & Carlberg 2014), distributions of ISM properties (Dobbs & Pringle 2010; Grand, Kawata & Cropper 2012a,b; Pettitt et al. 2020), motions of stars in spiral galaxies (Lindblad, Lindblad & Athanassoula 1996; Baba, Saitoh & Wada 2013; Ramón-Fox & Bonnell 2022), etc. These studies find that both the density wave theory and dynamic spirals are viable mechanisms for the formation of spiral arms.

Although non-trivial and difficult, there have been many attempts to distinguish the physical mechanism driving the formation of spiral arms from observations in the local Universe. The density wave theory adopts a fixed pattern speed across the disc, while the dynamic spirals induce the spiral arms to rotate with the disc at a radially decreasing angular velocity. The simplest detection of pattern speed is the corotation radius measured by the residual velocity maps of $^{12}C^{16}O$ and H I (Elmegreen, Elmegreen & Seiden 1989; Canzian 1993; Sempere et al. 1995), although this method is highly subject to measurement uncertainties. Peterken et al. (2019) detect the pattern speed by mapping the ongoing star formation and previously formed young stars as a direct test of the density wave theory. Another indirect method to determine the pattern speed is to detect the location of spiral-shaped shock waves (hereafter spiral shocks). The density wave theory predicts spiral shocks to be found on one side of the stellar potential within the corotation radius and on the opposite side outside the corotation radius. This results in an offset whose width is determined by the difference between pattern speed and material speed. In the dynamic spiral theory, we do not expect an offset on both sides of the spiral arms, as the material in the disc does not cross the spiral arm potential. Therefore, the distributions of gas-phase ISM properties and stellar populations are different depending on the assumed theory, which enable us to interpret the observations and understand the origin of spiral arms in the observed galaxies. This method has been applied to several nearby galaxies (e.g. Egusa, Sofue & Nakanishi 2004; Tamburro et al. 2008; Egusa et al. 2009; Pour-Imani et al. 2016; Abdeen et al. 2022), but not all observed galaxies are consistent with the prediction of the density wave theory (Foyle et al. 2011).

Integral field spectrographs (IFS) enable investigation into the radial and azimuthal distributions of stellar and gaseous ISM properties of galaxies. Large IFS surveys provide spatially resolved distributions of oxygen abundances, kinematics, and stellar populations (Falcón-Barroso et al. 2006; Marino et al. 2012; Rodríguez-Baras et al. 2018; Kreckel et al. 2019; Grasha et al. 2022; Chen et al. 2023), to constrain the formation and evolution of spiral galaxies. These studies provide unprecedented insight into the dynamics and metal variations of spiral galaxies in the local Universe. However, most IFS studies of spiral galaxies are limited to spirals in the local Universe, leaving a gap in our understanding of spiral patterns in high-redshift galaxies, when the very first galaxies settled down to develop spiral features. Even though observations have found the existence of spiral galaxies up to $z \sim 2$ (Law et al. 2012; Margalef-Bentabol et al. 2022), the formation of these spiral galaxies remains mysterious. The formation of spiral arms is assumed to happen in thin stable discs (Toomre 1977; Sellwood & Carlberg 2014) while galaxy discs are thicker, more gas rich, and less stable at higher redshifts (Crain et al. 2015; Wisnioski et al. 2015). The effects of the ISM become increasingly important in the build-up of spiral arms at higher redshifts (Wada, Baba & Saitoh 2011; Ghosh & Jog 2016). Spiral arms are also sensitive to environmental effects, including gas

Downloaded from https://academic.oup.com/mnras/article/527/2/2991/7339769 by guest on 22 July 2026

accretion and galaxy mergers (Wada, Baba & Saitoh 2011; Martig et al. 2012; Dobbs & Baba 2014). To understand the physics of spiral formation and when it dominates the star formation activities in star-forming galaxies, we need to push detailed observations to higher redshifts. Using spatially resolved IFS data targeting galaxies at a higher redshift, it is possible to discriminate density wave theory/dynamic spirals at an earlier stage of the formation of spiral galaxies.

Taking advantage of the adaptive optics of the Multi-Unit Spectroscopic Explorer (MUSE), the Middle Ages Galaxy Properties with Integral Field Spectroscopy (MAGPI; Foster et al. 2021) survey is carried out to target 60 massive galaxies and their satellites at $0.25 < z < 0.35$ (3–4 Gyr ago). Since the dynamical, morphological, and chemical properties of galaxies undergo significant transformation at $z \sim 0.3$, the MAGPI survey gives an important window in the cosmic timeline and fills up the gap in our understanding of the build-up of spiral features. The spatial resolution of MAGPI, which reaches 0.6–0.8 arcsec (full width at half-maximum – FWHM), enables us to distinguish the spiral arms and the interarms without the use of gravitational lensing. In this work, we study the two-dimensional distributions of different ISM properties and stellar populations in two spiral galaxies at $z \sim 0.3$ at a high spatial resolution, shedding light on the origin and growth of spiral arms. This paper demonstrates the feasibility of tracing ISM properties and their linkage to stellar spiral structures at $z \sim 0.3$, with a plan to expand the study to the full MAGPI spiral sample upon completion of the full data set.

In this paper, we present our first work on exploring spiral galaxies with IFS observations at $z \sim 0.3$. We introduce our sample in Section 2. We present our analysis of two gas ISM properties and stellar age in Section 3, and the results are then discussed in Section 4. Throughout this paper, we adopt the Chabrier (2003) initial mass function (IMF), and a flat cosmology with $\Omega_\Lambda = 0.7$, $\Omega_\mathrm{m} = 0.3$, and $H_0 = 70$ km s^{-1} kpc^{-1}.

2 DATA AND SAMPLE

2.1 Data

We use the observational data from the MAGPI[1] survey (35 fields at the time of starting this work, out of 56 MAGPI fields). MAGPI is a large program on the European Southern Observatory Very Large Telescope (VLT) that is still in progress at the time of writing (Program ID: 1104.B-0536). The observations are achieved through 56 × 4.4 h on-source exposures of independent fields with ground-layer adaptive optics (GLAO) on VLT/MUSE. The MAGPI sample is also supplemented with two archival MUSE fields of massive clusters at $z \sim 0.3$: Abell 370 and Abell 2744.

The science goals, design, and observing technique are described in detail in Foster et al. (2021). In brief, the survey aims to reveal and understand the physical processes responsible for the rapid transformation of galaxies at intermediate redshift ($z \sim 0.3$), by mapping the detailed properties of stars and the ionized gas in galaxies. MAGPI will provide constraints on understanding the role of gas accretion and merging and tracing the metal mixing history of galaxies. It has a comparable *physical* spatial resolution to local surveys [∼1–4 half-light radius/point spread function (PSF) FWHM; Foster et al. 2021] such as the Sydney-Australian-Astronomical-Observatory Multi-object Integral-Field Spectrograph (SAMI; Croom et al. 2021) and Mapping Nearby Galaxies at Apache Point Observatory (MaNGA; Bundy et al. 2015) surveys.

MAGPI uses the wide-field mode, yielding a ∼1 × 1 arcmin^2 field of view (FOV) sampled by 0.2 × 0.2 arcsec^2 spatial pixels (henceforth spaxels). The wavelength covers 4700–9350 Å and the spectral sampling is 1.25 Å spaxel^{-1}. The GLAO system ensures that all MAGPI targets are observed with an effective seeing of 0.65 arcsec FWHM in *V* band, or better. For each primary target, the total on-source integration time per field is 4.4 h, which ensures a signal-to-noise ratio (SNR) of 5 Å^{-1} per resolution element around 6000–6500 Å in the stellar continuum for individual spaxels at the half-light radius (R_e).

The data reduction process is briefly described in Foster et al. (2021) and will be provided in further detail in Mendel et al. (in preparation). The raw data are processed using PYMUSEPIPE[2] (Weilbacher et al. 2020). The final processing of the individual MUSE science exposures is performed outside of the standard pipeline, using CUBEFIX (Cantalupo et al. 2019) and Zurich Atmosphere Purge (ZAP) sky-subtraction software (Soto et al. 2016). The synthetic white-light (i.e. collapsed MUSE spectrum), *r*- and *i*-band images for each field are created using the MPDAF[3] python package. The PROFOUND package (Robotham et al. 2018) is an image analysis package applied to the white-light images to detect objects and to produce a preliminary segmentation map. PROFOUND is also used on *r*- and *i*-band images created from the MUSE data cubes for photometric parameters.

2.2 Sample description

From the 35 observation-completed MAGPI fields (2022 October), we find 12 non-merging galaxies that prominently show grand-design or multi-armed spiral features from visual inspection. We exclude merging spiral galaxies to remove complexities that could be introduced to the stellar and gas properties from tidal interactions. Tidally driven spiral arms are not discussed in this work. Fig. 1 shows the coloured images of our pilot sample including two three-armed face-one spiral galaxies: MAGPI 1202197197 (left of Fig. 1, hereafter SG 1202) and MAGPI 1204198199 (right of Fig. 1, hereafter SG 1204). The pilot sample has the largest R_e and the highest SNR among the 12 non-merging spiral galaxies, which allows for a detailed study and comparison between arm and interarm regions without the need for binning. This paper aims to demonstrate the feasibility of tracing spectral parameters and their linkage to spiral structures at $z \sim 0.3$. In our next paper, we will apply the methodology to the full MAGPI survey upon the completion of observation. The two spiral galaxies are part of a group according to the Galaxy And Mass Assembly (GAMA) galaxy group catalogue (G^{3}Cv1; Robotham et al. 2011) that indicates they are presumably under environmental effects from their companion galaxies. The physical parameters of galaxies in our pilot sample are listed in Table 1.

3 DATA ANALYSIS AND RESULTS

In this section, we present our analysis of the reduced MAGPI data including the spectral fitting processes, spaxel selection, the definition of spiral arms and interarm regions, and the measure of spectral parameters. Our goal is to constrain the origin of spiral features by studying the impacts of spiral arms on the gas ISM properties and

[1] https://magpisurvey.org

[2] https://github.com/emsellem/pymusepipe

[3] https://github.com/musevlt/mpdaf

Downloaded from https://academic.oup.com/mnras/article/527/2/2991/7339769 by guest on 22 July 2026

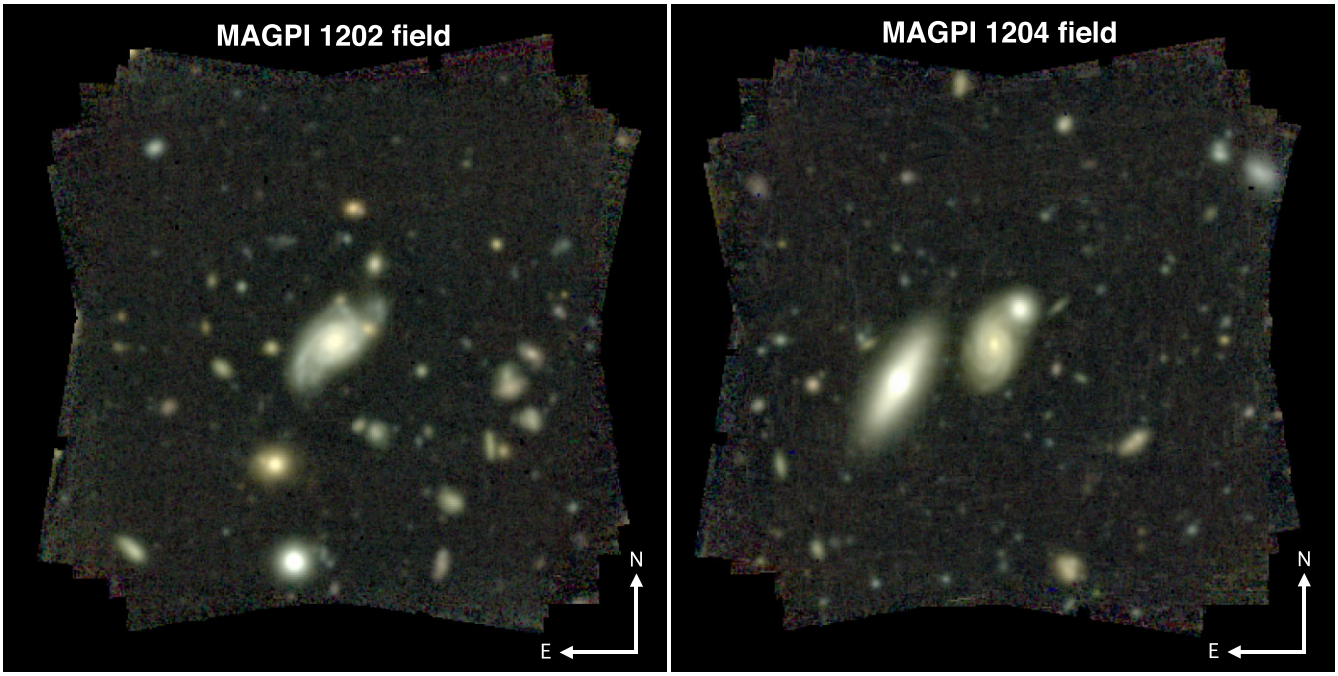

Figure 1. MUSE $g_{\rm mod}ri$ [4] composite images of the two well-defined spiral galaxies at the centre of each FOV of the MAGPI 1202 (left) and MAGPI 1204 (right) fields. Our pilot sample consists of MAGPI 1202197197 (hereafter SG 1202, at $z \simeq 0.2919$) and MAGPI 1204198199 (hereafter SG 1204, at $z \simeq 0.3163$), which are the large spiral galaxies located at the centre of each field. The companion galaxy to the north-west of SG 1204 is a foreground galaxy at $z \simeq 0.254$.

Table 1. Physical parameters of our pilot sample galaxies from MAGPI in this study. Column (1): galaxy name in the MAGPI survey and their short name in this work. Columns (2) and (3): J2000 coordinates of the galaxy in unit of degree. Columns (4) and (5): inclination and photometric position angle (PA) are measured with PROFOUND (Mendel, in preparation). Column (6): redshift measured from MARZ. Column (7): stellar mass of the spiral galaxies from Mun et al. (submitted), applying single population synthesis to stellar energy distribution fitting on the Hyper Suprime-Cam (HSC) images following Taylor et al. (2011). The total stellar mass is obtained by summing the stellar mass in each pixel within the dilated mask from PROFOUND. Column (8): half-light radius ($R_{\rm e}$) determined with PROFOUND on i-band images. Column (9): pitch angles of the spiral arms (see Section 3.3) are listed clockwise from the north arm.

Galaxy	RA (°)	Dec. (°)	Inclination (°)	PA (°)	Redshift	$\log(M_*/M_\odot)$	$R_{\rm e}$ (kpc)	Pitch angle (°)
(1)	(2)	(3)	(4)	(5)	(6)	(7)	(8)	(9)
MAGPI 1202197197 (SG 1202)	175.3388	−1.5825	56.5	132.6	0.2920	10.88 ± 0.01	9.23	29.1, 27.5, 20.4
MAGPI 1204198199 (SG 1204)	175.6612	−0.7943	46.9	175.0	0.3164	11.01 ± 0.01	10.09	16.7, 19.4, 21.0

stellar populations. We focus on the two-dimensional distributions of star formation rate (Section 3.5), gas-phase metallicity (Section 3.6), and stellar age (Section 3.7) in the following analysis.

3.1 Emission line fits

Two-dimensional spectral maps are obtained with GIST (Bittner et al. 2019), which is a pipeline with implemented PPXF (Cappellari & Emsellem 2004; Cappellari 2017) and PYGANDALF (Falcón-Barroso et al. 2006; Sarzi et al. 2006) routines. The GIST pipeline simultaneously extracts kinematics, emission lines, and stellar population properties from full spectral fitting. There are several unique customizations made (Battisti et al., in preparation; Mendel et al., in preparation) for its use with MAGPI data when fitting emission lines.

(i) A binning scheme is used where if the SNR of the continuum is too low for the adopted threshold for Voronoi bins, then a single integrated bin is adopted instead. Voronoi binning optimally preserves the maximum spatial resolution of two-dimensional data, given a constraint on the minimum SNR (Cappellari & Copin 2012). The continuum fitting is based on a binning scheme while the following emission line fits are on a spaxel level.

(ii) A modified version of PYGANDALF is implemented that

(a) employs three different sets of input parameters including the flux, velocity, and velocity dispersion, which is adjusted based on the best fit of the stellar component. The fitting that yields the lowest χ^2 is considered as the final fitting results for the gas component. This modification is tailored to effectively handle low SNR emission lines;

(b) estimates the errors on fluxes, velocities, and standard deviations for the emission lines, based on a Monte Carlo approach.

The emission line working group of the MAGPI survey adopts the light-weighted stellar templates from SSP_MIST_C3K_SALPETER (Conroy, private communication) and sets the multiplicative Legendre polynomial to 12. The emission lines are fit as a Gaussian function that is independent of the chosen IMF. The targeted SNR of the stellar continuum for Voronoi binning is 10. The emission line fits are carried out with a single component tied to the brightest

[4] $g_{\rm mod}$ covers part of the g band redder than 4700 Å.

Downloaded from https://academic.oup.com/mnras/article/527/2/2991/7339769 by guest on 22 July 2026

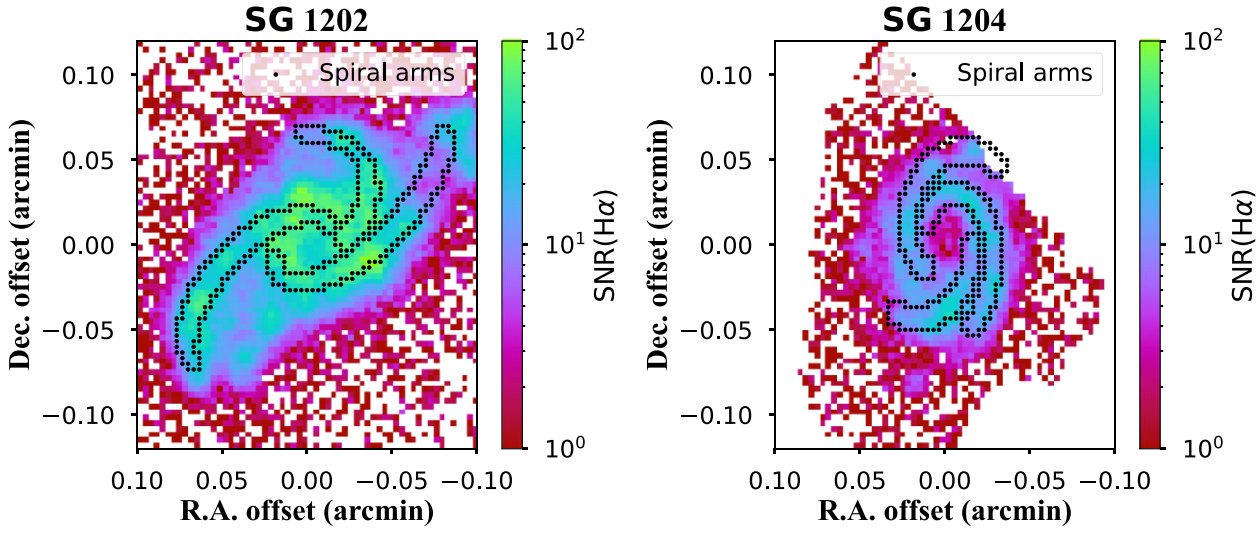

Figure 2. SNR maps of SG 1202 and SG 1204. Only spaxels with SNR > 3 in Hα and Hβ are selected for all the following analyses. The defined spiral arms are overplotted as black dots (see Section 3.3). The spiral arms show a higher SNR of Hα than the interarm regions.

line for the wavelength range covered at the galaxy redshift (i.e. Hα for $0 < z < 0.424$, [O III] λ5007 for $0.424 < z < 0.865$, and [O II] λ3729 for $0.865 < z < 1.507$). The line velocity for each spaxel is restricted to $\pm$600 km s^{-1} relative to the stellar continuum velocity of the nearest Voronoi bin. For each MAGPI field, Mendel et al. (in preparation) empirically measure the line spread function (LSF), which will be adopted in the following fitting processes. The spectral line data products, including [O II] $\lambda\lambda$3726, 3729, D_{4000}, Hβ (4861 Å), [O III] λ5007, Hα (6563 Å), and [N II] λ6584 used in this work, are made by the MAGPI team and will be publicly available in a forthcoming data release (Battisti et al., in preparation).

3.2 Spaxel selection criteria

To achieve a reliable scientific analysis of SG 1202 and SG 1204, we apply SNR > 3 limits (Fig. 2) to Hβ and Hα emission lines before extinction correction. The spaxels with SNR below 3 are excluded from all the following analyses. To ensure sufficient spaxels and accurate analysis, we establish a 3σ lower limit by assigning three times the noise as the new signal for [O III] λ5007 and [N II] λ6584 where if the spaxels have a SNR less than 3 (see section 2.6 of Rosario et al. 2016). In face-on spiral galaxies, H II regions with low scale height destroy the dust within birth clouds and therefore are predominantly affected by dust in the foreground (Wild et al. 2011). Thus, in this work, we apply the Milky Way extinction curve from Fitzpatrick et al. (2019) as

$$E(B-V) = 2.5 \times \left(\frac{\log_{10} \frac{(\mathrm{H}\alpha/\mathrm{H}\beta)_{\mathrm{obs}}}{(\mathrm{H}\alpha/\mathrm{H}\beta)_{\mathrm{int}}}}{k_{\mathrm{H}\beta} - k_{\mathrm{H}\alpha}} \right). \quad (1)$$

We adopt $R_v = 3.1$ to determine the k value at each wavelength and measure the colour excess $E(B-V)$ for all spaxels with SNR (Hα and Hβ) > 3. The $E(B-V)$ values are then used to calculate the intrinsic emission line fluxes F_{int} from the observed fluxes F_{obs} as

$$F_{\mathrm{int}} = F_{\mathrm{obs}} \times 10^{0.4 k_\lambda E(B-V)}. \quad (2)$$

The extinction-corrected fluxes are used in all the following analyses to measure the gas-phase metallicities (Section 3.6).

To limit our analyses to spaxels that arise predominantly from star formation (i.e. photoionization) and exclude spaxels excited mainly by hard components (e.g. shocks, active galactic nuclei – AGN), we use the Baldwin–Phillips–Terlevich (BPT) diagram (Baldwin, Phillips & Terlevich 1981) to separate spaxels based on different excitation mechanisms. Based on [N II] λ6584/Hα versus [O III] λ5007/Hβ, low-ionization nuclear emission-line regions (LINERs) and AGN are distinguished from the H II regions, which are powered primarily by photoionization (Kewley et al. 2001; Jin, Kewley & Sutherland 2022). We separate AGN/shock spaxels from photoionization by using the Kewley et al. (2001) demarcation line, which models the starburst galaxies with PEGASE v2.0 and STARBURST99 to derive the theoretical classification scheme for AGN and H II regions. Another work (Kauffmann et al. 2003b) presents an empirical demarcation line based on the properties of $\sim$120 000 nearby galaxies with the Sloan Digital Sky Survey. The spaxels beneath the Kauffmann et al. (2003b) demarcation line are interpreted to be purely star formation excited, while data over the theoretical Kewley et al. (2001) demarcation line predominately arise by AGN or LINER emission sources. A total of 1.1 per cent (0.8 per cent) spaxels in SG 1202 (SG 1204) lie above the Kewley et al. (2001) line, which are excluded in the following analyses.

3.3 Defining the spiral arms

We identify the spiral arms of our two galaxies with a combination of computer algorithms and manual checks, using the automated tool SPARCFIRE (Davis & Hayes 2014), which was developed based on Galaxy Zoo data (Lintott et al. 2008, 2011). To highlight the spiral features of our two galaxies at $z \sim 0.3$, we employ GALFIT to determine the optimal Sérsic component and subtract it from the white-light images. Following the deprojection process in section 3.3 of Grasha et al. (2017), we deproject the galaxy images based on the inclination and PA in Table 1 that are then set as the input of SPARCFIRE. The output of SPARCFIRE based on deprojected images is shown in Fig. A1: red spiral arms are identified as having positive pitch angles (clockwise), while blue arms have negative pitch angles (counterclockwise). As three continuous spiral arms are vividly observable in both the white-light images (Fig. 1), we only keep the

Downloaded from https://academic.oup.com/mnras/article/527/2/2991/7339769 by guest on 22 July 2026

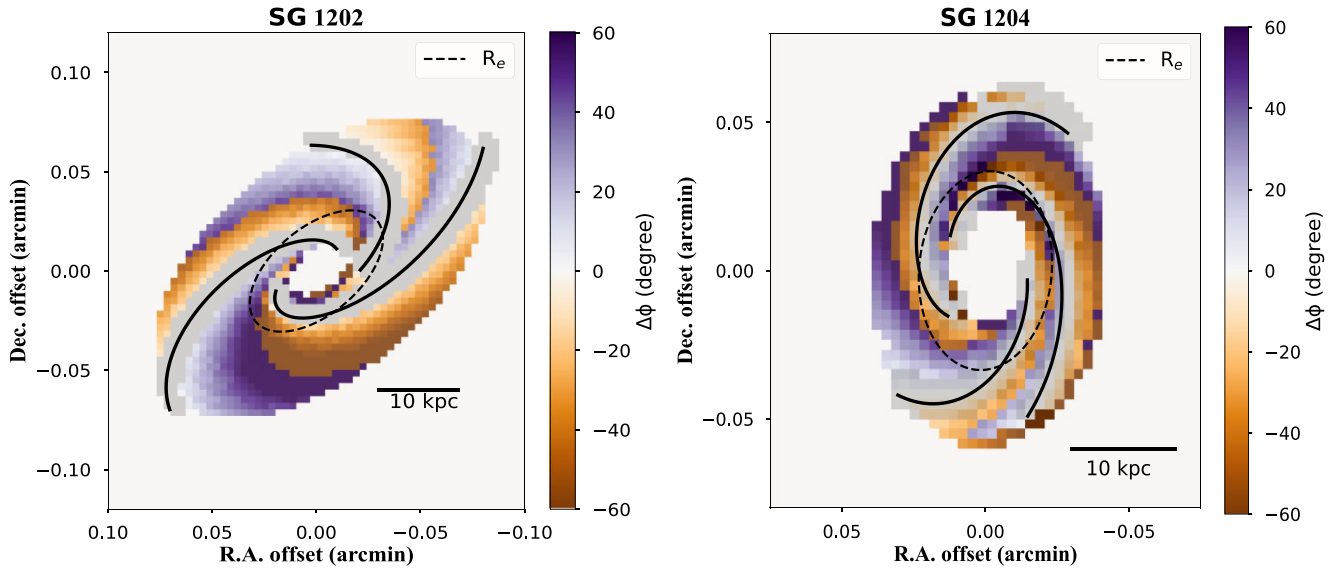

Figure 3. A measure of the angular azimuthal distance to the nearest spiral arm (grey pixels) at a constant galactocentric distance ($\Delta\phi$) of SG 1202 (left) and SG 1204 (right), overplotted with the spiral arm ridge lines. We define $\Delta\phi$ only for the spaxels located at the galactocentric distance where three spiral arms are present, thus there is an absence of $\Delta\phi$ in the central region. Interarm spaxels with negative (positive) $\Delta\phi$ are classified as downstream (upstream), colour coded as orange (purple). $1R_e$ is shown as the dashed ellipse.

three longest spiral arms from the output of SPARCFIRE for both spiral galaxies. As a secondary step, we fine-tune the starting and ending radii of the spiral ridge lines to improve their alignment with the observed white-light images. The final adopted spiral arm ridge lines are presented in Fig. 3, overplotted on the $\Delta\phi$ map, which represents the angular azimuthal distance to the nearest spiral arm at a constant galactocentric distance (Section 3.4). The typical spiral arm width in the Milky Way is ∼1 kpc (Reid et al. 2014). We demarcate the width of spiral arms as 2 kpc in the MAGPI survey, taking the beam-smearing effects (0.6–0.8 arcsec; FWHM) into account. We show the boundary of the spiral arms as black dots in Fig. 2.

3.4 Definition of azimuthal distance $\Delta\phi$

Depending on the physical mechanisms that assemble spiral arms, density wave theory or dynamic spirals, stellar populations, and gas in the ISM between both sides of the spiral arms are expected to show different behaviours, which can be used to constrain the origin of the spiral features. The spatially resolved IFS data from our MAGPI observations allow us to compare the ISM properties between the spiral arm and interarm regions and differences between downstream and upstream in the interarm regions. To identify the different parts of interarms, we define $\Delta\phi$ that measures the azimuthal distance to the nearest spiral arm. We assign

$$\Delta\phi_i = -\min(|\phi_j - \phi_i|) \tag{3}$$

when pixel i is on the leading edge of the nearest spiral arm and assign

$$\Delta\phi_i = \min(|\phi_j - \phi_i|) \tag{4}$$

when pixel i is on the trailing edge of the nearest spiral arm. The pixel i is the targeted pixel and the pixel j is the pixel within the spiral regions at the same galactocentric distance (within 0.5 kpc uncertainty).

With the defined spiral arm ridge lines, the $\Delta\phi$ maps of SG 1202 and SG 1204 are presented in Fig. 3. The interarm spaxels with negative (positive) $\Delta\phi$ are classified as downstream (upstream). In the following sections, we will analyse ISM properties and stellar populations as tests of the density wave theory.

3.5 Star formation rate

Star formation is one of the major drivers of galaxy evolution and is the process that enriches the ISM with metals. Young, massive stars produce copious amounts of ionizing photons that are observed in emission nebular lines (e.g. Hα). Stars more massive than ∼10 $M_\odot$ produce a measurable ionizing photon flux and only live ∼10 Myr, providing a sensitive indicator of young, massive stellar populations. In this work, we adopt the star formation rate (SFR) prescription from Kennicutt (1998) to measure the SFR for each spaxel:

$$\mathrm{SFR}\,(M_\odot\,\mathrm{yr}^{-1}\,\mathrm{cm}^{-2}) = 7.9\times10^{-42}\times F_{\mathrm{H}\alpha}\,(\mathrm{erg\,s}^{-1}\,\mathrm{cm}^{-2}), \tag{5}$$

where $F_{\mathrm{H}\alpha}$ is the flux of Hα per spaxel after dust correction (Section 3.2). For consistency with the MAGPI survey, we adopt the Chabrier (2003) IMF. Following Bernardi et al. (2010), the SFR is divided by $10^{0.25}$ to convert the IMF from the original Salpeter (1955) to our preferred Chabrier (2003) IMF.

We calculate the spatially resolved SFR surface density (Σ_{SFR}) as follows:

$$\Sigma_{\mathrm{SFR}}\,(M_\odot\,\mathrm{yr}^{-1}\,\mathrm{kpc}^{-2}) = \frac{\mathrm{SFR}\times10^{-0.25}}{[D_{\mathrm{A}}\,(\mathrm{kpc})\times0.2]^2}, \tag{6}$$

where D_{A} is the angular diameter distance of the galaxy and 0.2 arcsec pixel^{-1} is the pixel scale of the MAGPI survey.

The higher Σ_{SFR} in the spiral arms than in the interarm regions observed in both SG 1202 and SG 1204 shows that the enhanced star formation is occurring within the spiral arms (see derived Σ_{SFR} maps in Fig. 4). Fig. 5 compares the radial profiles of Σ_{SFR} in the $\Delta\phi < 0$ (downstream; orange) and $\Delta\phi > 0$ (upstream; purple) regions as a function of deprojected radial distance. In SG 1202 (left panel of Fig. 5), we observe a generally higher Σ_{SFR} in the downstream (orange) than in the upstream (purple) between $1R_e$ and $2R_e$ (∼10–20 kpc).

Downloaded from https://academic.oup.com/mnras/article/527/2/2991/7339769 by guest on 22 July 2026

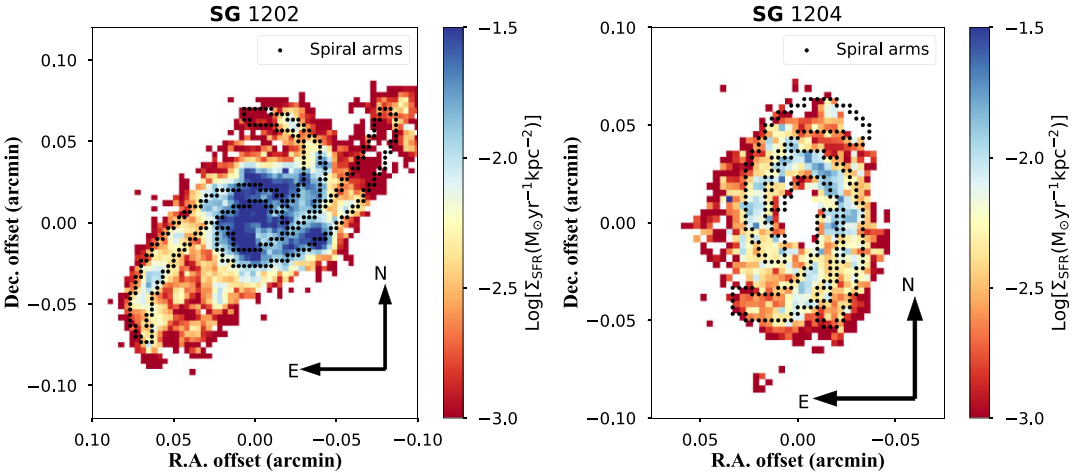

Figure 4. Σ_{SFR} maps based on dust-corrected Hα flux of SG 1202 (left) and SG 1204 (right), overplotted with the boundary of defined spiral arm regions. Higher (blue) Σ_{SFR} is predominantly located within the arm regions.

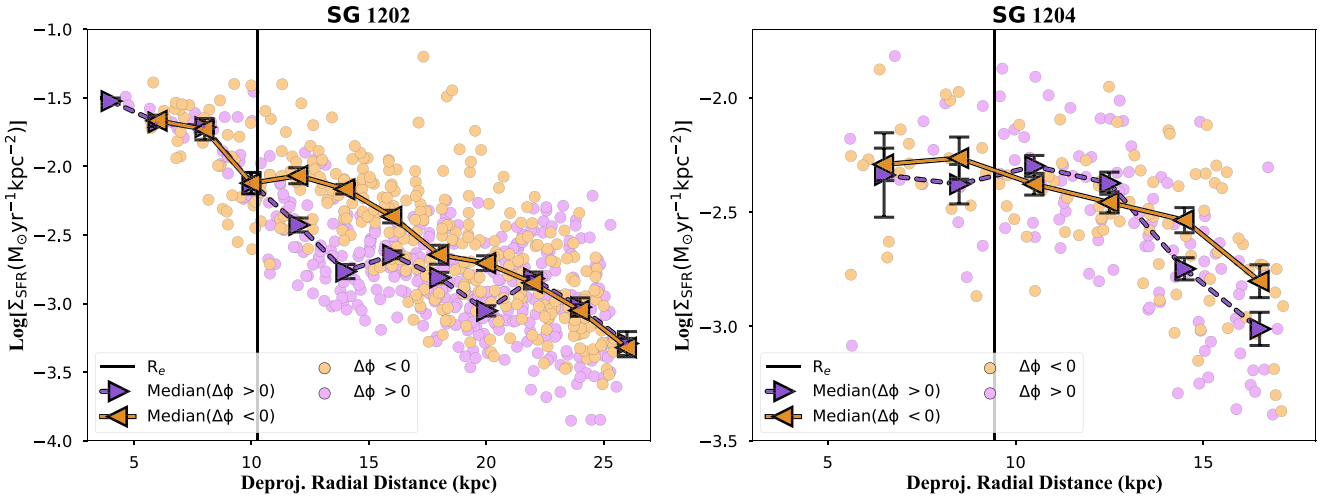

Figure 5. Radial profiles of Σ_{SFR} of SG 1202 (left) and SG 1204 (right), colour coded by their location in the spiral galaxy: $\Delta\phi < 0$ (downstream; orange) and $\Delta\phi > 0$ (upstream; purple). The x-axis is the radial distance to the galaxy centre after deprojection (following Grasha et al. 2017). The medians of each 1 kpc elliptical bin are marked as triangles with 1σ error bars. The vertical solid line marks the location of $1R_e$ in each galaxy. Significantly higher Σ_{SFR} is observed in the downstream ($\Delta\phi < 0$; orange) of SG 1202 than the upstream ($\Delta\phi > 0$; purple) in the range $1 < R/R_e < 2$, whereas SG 1204 shows comparable Σ_{SFR} in the $\Delta\phi < 0$ (downstream) and $\Delta\phi > 0$ (upstream) regions across all galactocentric distances.

The Σ_{SFR} in the downstream ($\Delta\phi < 0$) of SG 1204 (right panel of Fig. 5) is indistinguishable from the upstream ($\Delta\phi > 0$) at all galactocentric distances and has no noticeable change at $1R_e$, unlike SG 1202. The Σ_{SFR} radial trends in different $\Delta\phi$ of SG 1202 are consistent with the theoretical expectations from the quasi-stationary density wave theory (Section 1). Our data indicate more intense star formation located on the leading side of the spiral arm, compared to the trailing side between $1R_e$ and $2R_e$. The absence of an offset in Σ_{SFR} across all radii of SG 1204 can be the consequence of the galaxy having a tighter pitch angle (last column in Table 1) compared to SG 1202. This scenario is further discussed in Section 4 and requires a larger observational sample to investigate.

3.6 Gas-phase metallicity

The spatial distribution of gas-phase metallicities is a critical component for understanding the physical evolution of spiral galaxies, including their star formation history and mixing processes in the ISM (Kewley, Nicholls & Sutherland 2019; Maiolino & Mannucci 2019; Li et al. 2021; Sharda et al. 2023). Oxygen is the most abundant metal element in the Universe, which is mostly produced on short time-scales by Type II supernovae along with other α elements. In this work, we measure the oxygen abundances to represent the gas-phase metallicities of our galaxies utilizing the N2O2 diagnostic (Kewley & Dopita 2002). The N2O2 diagnostic uses three bright optical lines: [N II] λ6584/[O II] $\lambda\lambda$3726, 3729. The combination of [N II] λ6584 and [O II] $\lambda\lambda$3726, 3729 requires a reliable extinction correction that is carried out in Section 3.2. The N2O2 diagnostic is insensitive to the ionization parameter or ionizing spectrum hardness (Zhang et al. 2017; Kewley, Nicholls & Sutherland 2019). As such, it is also insensitive to the diffuse ionized gas that permeates outside of H II regions. It makes N2O2 an ideal metallicity diagnostic for our observations. We utilize the python package PYMCZ (Bianco et al. 2016) to measure the gas-phase metallicities and uncertainties with a Monte Carlo method.

Downloaded from https://academic.oup.com/mnras/article/527/2/2991/7339769 by guest on 22 July 2026

We present the metallicity radial profiles, colour coded by their 1σ uncertainty, in the left column of Fig. 6. We show the 2D metallicity maps in the middle column of Fig. 6. The observed negative radial gradient (-0.069 ± 0.002 dex/R_e) in SG 1202 is indicative of typical inside-out formation, commonly seen in local spiral galaxies (Sánchez-Menguiano et al. 2018; Chen et al. 2023), while the flat metallicity gradient (-0.014 ± 0.007 dex/R_e) in SG 1204 suggests strong gas mixing that could be induced by recent interactions or cosmic gas accretion (Kewley et al. 2010; Rupke, Kewley & Barnes 2010a; Rupke, Kewley & Chien 2010b; Perez, Michel-Dansac & Tissera 2011; Vollmer et al. 2012). The shallower gradient in the Σ_{SFR} profile of SG 1204 compared to the one of SG 1202 is also suggestive of a stronger mixing process, which can cause the absent azimuthal variation in the metallicity of SG 1204 (further discussed in Section 4).

From the 2D metallicity map of SG 1202 (top middle panel of Fig. 6), we observe significantly higher metallicities (redder colour) in the inner region that is consistent with the negative metallicity gradient. We notice bluer spaxels (low metallicities) concentrated within the spiral arms than the interarms. In the 2D metallicities map of SG 1204 (bottom middle panel of Fig. 6), we find comparable metallicity across the disc region that is in line with the observed shallow metallicity gradient. We do not find a distinctive difference in the metallicity between spiral arms and interarms that could be attributed to the tighter spiral arms.

Azimuthal metallicity variation can inform us of how metals are mixed in with their neighbouring ISM when gas and stars are rotating in their orbits (Ho et al. 2017). The IFS data of MAGPI allow us to study small-scale variations (0.6–0.8 arcsec FWHM) present in the gas-phase metallicity, which is typically a much weaker trend than the global radial gradient. To calculate the residual metallicity maps $\Delta\log(O/H)$, we first calculate the weighted averages of each 1 kpc elliptical bin to represent the radial gradients and subtract that from the metallicity maps. Positive (negative) residual $\Delta\log(O/H)$ indicates higher (lower) $12 + \log(O/H)$ compared to spaxels at the same galactocentric distance; this allows us to study the azimuthal variations, if present.

In SG 1202 (top right panel of Fig. 6), we find higher $\Delta\log(O/H)$ in the inner region of the north-west spiral arm, while the north arm and east arm are systematically dominated by negative $\Delta\log(O/H)$. It is challenging to directly compare the metallicity between the arm and interarm regions based on the $\Delta\log(O/H)$ map of SG 1204 (lower panel of Fig. 6), since the scale of $\Delta\log(O/H)$ is comparable to the typical uncertainty of gas-phase metallicity (0.1 dex). We perform a Kolmogorov–Smirnov (KS) test to compare the distributions of $\Delta\log(O/H)$ in the arm and interarms. The results of the KS test and the p-values are shown in Table 2 and summarized below. The p-value measures the probability of the null hypothesis that the two samples are drawn from the same distribution for which a significance level of 1 per cent is commonly used. It is worth mentioning that the p-values are an overrepresentation of how different the distributions truly are because the large sample size will cause the KS test to have very high power for discerning small differences in the distributions. In addition, the KS test does not take into account the error in the parameters (Lazariv & Lehmann 2018).

For SG 1202, the p-value (1.7×10^{-4}) of the KS test suggests that $\Delta\log(O/H)$ has a different distribution in the arms compared to the interarms. We find generally negative $\Delta\log(O/H)$ in the spiral arms with an error-weighted average of $-3.9 \pm 1.0 \times 10^{-3}$. This is lower than the interarms with an error-weighted average of $4.3 \pm 1.0 \times 10^{-3}$. SG 1204 has spiral arms that are significantly tighter (with a smaller pitch angle) than SG 1202. The KS test suggests that it is possible that the $\Delta\log(O/H)$ distributions in the arms and interarms are drawn from the same distribution (with a p-value of 6.8×10^{-2}; Table 2). The difference in the $\Delta\log(O/H)$ of SG 1202 and SG 1204 is implied in the more wounded spiral arms of SG 1204, coming along with stronger mixing processes. We discuss the physical mechanisms driving this difference in detail in Section 4.

Based on the measurement of $\Delta\phi$ (Section 3.4), we compare the $12 + \log(O/H)$ on different sides of the spiral arms across different radii (Fig. 7). In SG 1202, we observe marginally higher metallicities in the upstream (purple; $\Delta\phi > 0$) than in the downstream (orange; $\Delta\phi < 0$), outside 1σ uncertainty and within 3σ uncertainty. The p-value (4.7×10^{-3}) from the KS test strongly rejects the null hypothesis that the $12 + \log(O/H)$ in the downstream and upstream are drawn from the same distribution. The observed azimuthal variation in the metallicity of SG 1202 suggests that the origin and development of spiral arms in this galaxy are consistent with the density wave theory. However, we find that the metals in the ISM are well mixed in the interarms of SG 1204. The p-value (4.1×10^{-1}) from the KS test supports the same distribution of $12 + \log(O/H)$ on both sides of the spiral arms of SG 1204. The absence of azimuthal metallicity variation in SG 1204 is consistent with the dynamically driven spiral arms. Besides, the different azimuthal metallicity distributions in the SG 1202 and SG 1204 can be attributed to the tighter pitch angle of SG 1204 that implies a shorter (more efficient) mixing time-scale and higher ISM mixing effects.

3.7 Stellar age

In addition to the distribution of the ISM gas, the distributions of stellar populations also hint at the origin and evolution of spiral galaxies. In this work, we constrain the stellar age with D_{4000}, which is a continuum feature that occurs around 4000 Å due to the absorption in the atmosphere within older stellar populations (Noll et al. 2009). Because of our limited spectral quality, we are unable to operate spectrum energy distribution (SED) fitting on a spaxel scale. To get a sufficient SNR for SED fitting, we must bin the MAGPI data into a coarser spatial resolution, rendering the spiral arms and interarm regions no longer distinguishable.

Based on the GIST stellar continuum fits (Section 3.1), we determine the D_{4000} value on a spaxel level following:

$$D_{4000} = \frac{\mathrm{Flux}_{\mathrm{rest\ frame}}(4050\text{–}4250\ \text{Å})}{\mathrm{Flux}_{\mathrm{rest\ frame}}(3750\text{–}3950\ \text{Å})}. \quad (7)$$

We exclude spaxels with D_{4000} uncertainty larger than 0.5 in the following analysis of stellar age.

Consistent with inside-out galaxy formation, we find negative gradients in the D_{4000} of SG 1202 and SG 1204 (left panels of Fig. 8), with a flattening trend outside $1R_e$. In the middle panels of Fig. 8, we present the 2D maps of D_{4000}, overplotted with the boundary of the spiral arms. In SG 1202, we observe slightly lower D_{4000} (bluer spaxels) in the spiral arms compared to the interarms outside $1R_e$, which indicates younger stellar age in the arm regions than the interarms. These results are in agreement with the observed higher Σ_{SFR} within the arm regions of SG 1202 (Section 3.5). However, in SG 1204, we have difficulty comparing the D_{4000} within the arm regions and the close interarms based on the tight spiral features. We carry on our study of D_{4000} by introducing the D_{4000} residual in the next paragraph.

To explore the azimuthal variation of D_{4000}, we subtract the radial gradient from the original D_{4000} maps (middle panels of Fig. 8) to create the D_{4000} residual maps (ΔD_{4000}; right panels of Fig. 8). The radial gradient is represented by the weighted average of each 1 kpc ellipti-

Downloaded from https://academic.oup.com/mnras/article/527/2/2991/7339769 by guest on 22 July 2026

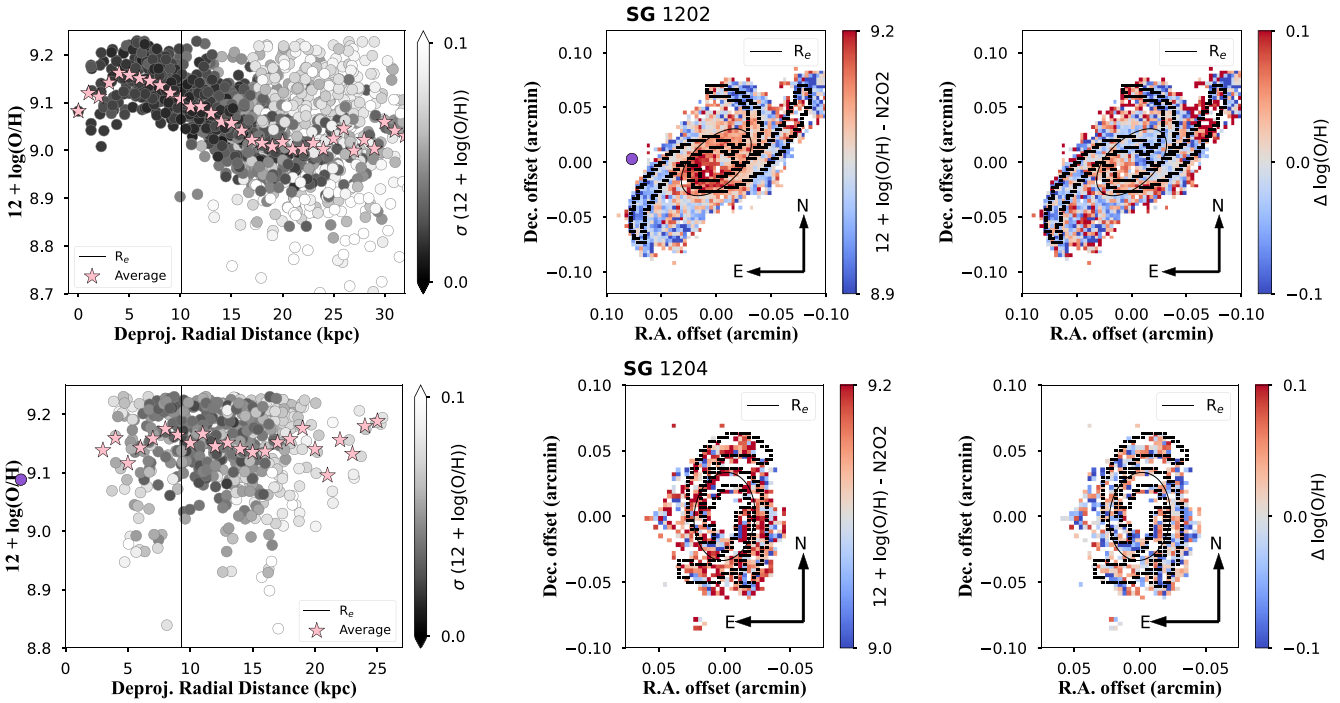

Figure 6. Left panels: radial profiles of gas-phase metallicity of SG 1202 (top) and SG 1204 (bottom), colour coded by 1σ uncertainty. The vertical solid line delimits the $1R_e$. The pink star symbols are the weighted average of each 1 kpc elliptical bin. We observe a steep-shallow metallicity gradient in SG 1202 that is consistent with the simulation in Garcia et al. (2023) and local observations in Grasha et al. (2022) and Chen et al. (2023). We find a flat metallicity gradient in SG 1204 that indicates strong mixing effects. Middle panels: gas-phase metallicity maps 12 + log(O/H) of SG 1202 (top) and SG 1204 (bottom), overplotted with the boundary of spiral arms and an ellipse at the location of $1R_e$. We find a concentration of blue spaxels with low metallicity within the spiral arms of SG 1202 but no systematic difference between arms and interarms of SG 1204. Right panels: residual metallicity maps Δlog(O/H) of SG 1202 (top) and SG 1204 (bottom) obtained by subtracting the radial gradient (pink star symbols in the left column) from the metallicity maps (middle), overplotted with the boundary of spiral arms and ellipse at $1R_e$. We observe a lower Δlog(O/H) in the arm regions of SG 1202, but no significant azimuthal variation in SG 1204. This difference can be a consequence of efficient mixing that is implied in the flat metallicity gradient of SG 1204.

Table 2. The p-values of KS test on Δlog(O/H) – first and third rows – and ΔD_{4000} – second and fourth rows – in the spiral arms versus interarms (column 3), $\Delta\phi < 0$ (downstream) versus $\Delta\phi > 0$ (upstream) in column 4. The populations whose p-values from the KS test are larger than 1 per cent are highlighted in bold.

Galaxy	Gas and stellar properties	Arms versus interarms	$\Delta\phi < 0$ versus $\Delta\phi > 0$
SG 1202	Δlog(O/H)	1.7×10^{-4}	4.7×10^{-3}
	ΔD_{4000}	2.0×10^{-6}	$\mathbf{1.4 \times 10^{-1}}$
SG 1204	Δlog(O/H)	$\mathbf{6.8 \times 10^{-2}}$	$\mathbf{4.1 \times 10^{-1}}$
	ΔD_{4000}	3.6×10^{-3}	$\mathbf{3.9 \times 10^{-1}}$

cal bin (light pink star symbols in the left panels of Fig. 8). A positive ΔD_{4000} indicates an older stellar age than the average stellar age at the same galactocentric distance. Both SG 1202 and SG 1204 show a generally negative ΔD_{4000} (blue spaxels) within the spiral arms. The KS test results (p-value of 2.0×10^{-6}) indicate that the distribution of ΔD_{4000} in the spiral arms of SG 1202 is significantly different from the distribution in the interarms. Similarly, SG 1204 shows a ΔD_{4000} variation between arms and interarms, with a p-value of 3.6×10^{-3}. The concentration of negative ΔD_{4000} (younger stellar population) in the arm region of SG 1202 and SG 1204 is in line with the expectation from the observed higher Σ_{SFR} in the arms (Section 3.5). We will further discuss the connection among different tracers in Section 4.

Taking advantage of the high spatial resolution of MUSE, we compare the D_{4000} in the downstream and upstream across different radii (Fig. 9). We observe no distinguishable D_{4000} offset, within 1σ uncertainty, between downstream and upstream in SG 1202 from the radial profiles (Fig. 9). The p-values from the KS test on the ΔD_{4000} of downstream versus upstream (1.4×10^{-1} for SG 1202 and 3.9×10^{-1} for SG 1204) indicate the ΔD_{4000} on both sides of the spiral arms are consistent with being drawn from the same distribution. The offset of the medians on the outskirt of SG 1204 could be attributed to the limited number of available spaxels.

To summarize, the open-armed spiral galaxy SG 1202 shows higher Σ_{SFR} (left panel of Fig. 5) and lower gas-phase metallicity (left panel of Fig. 7) in the downstream ($\Delta\phi < 0$; orange) than the upstream ($\Delta\phi > 0$; purple). As a proxy for the stellar age within SG 1202, D_{4000} does not show a distinguishable offset between both sides of the arm regions (left panel of Fig. 9). The tightly wounded spiral galaxy SG 1204 presents no significant differences in the Σ_{SFR} (right panel of Fig. 5), 12 + log(O/H) (right panel of Fig.

Downloaded from https://academic.oup.com/mnras/article/527/2/2991/7339769 by guest on 22 July 2026

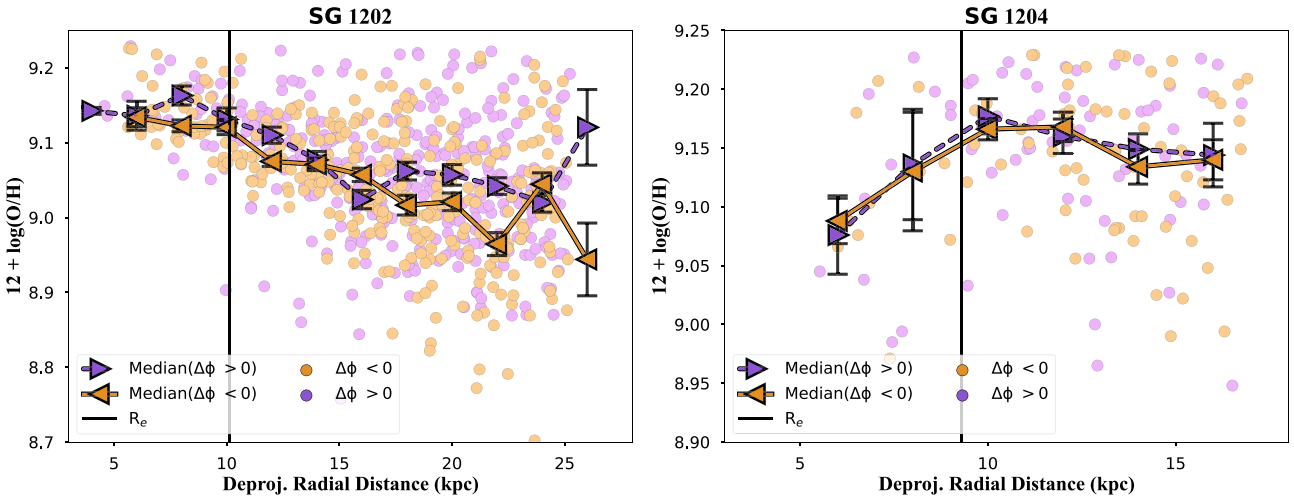

Figure 7. Comparison of metallicity in the $\Delta\phi < 0$ (downstream; orange) versus $\Delta\phi > 0$ (upstream; purple) spaxels in SG 1202 (left) and SG 1204 (right). The large solid triangles are the medians of each 1 kpc elliptical bin, with 1σ error bars. $1R_e$ is marked as vertical solid lines. The KS test suggests the $12 + \log(O/H)$ in the downstream and upstream of SG 1202 are possibly drawn from different distributions, while agreeing that the $12 + \log(O/H)$ on both sides of the spiral arms in SG 1204 are possibly drawn from the same distribution.

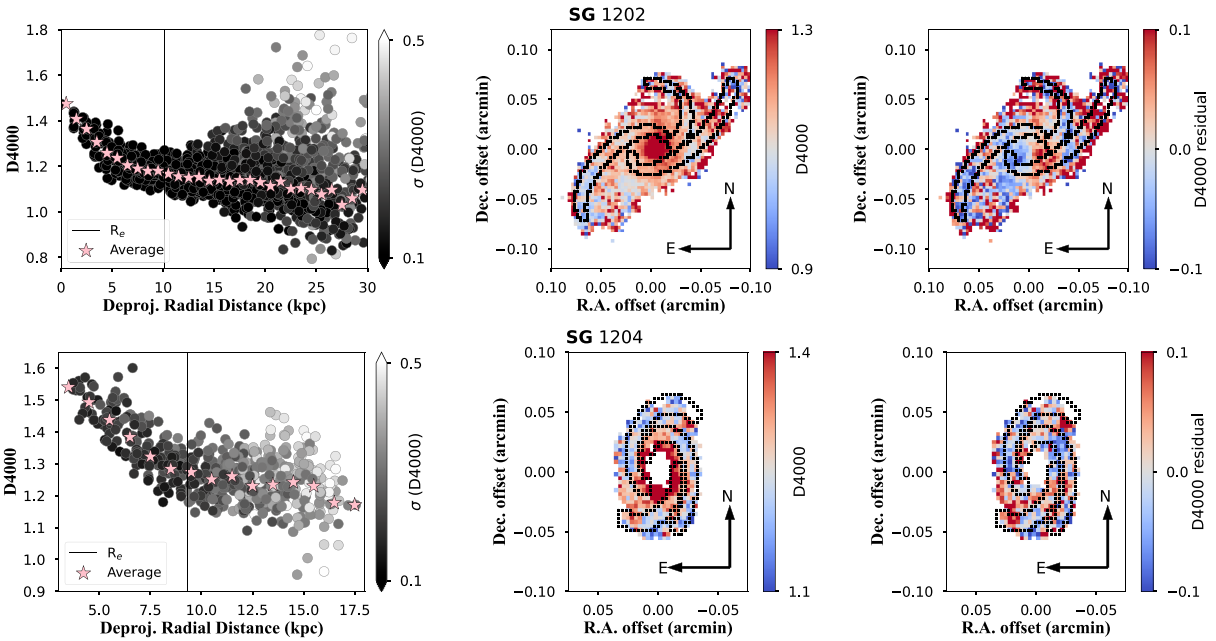

Figure 8. Radial profiles colour coded by 1σ uncertainty (left), 2D maps (middle), and residual maps (right) of D_{4000} in SG 1202 (top) and SG 1204 (bottom). The residual maps are calculated by subtracting the weighted average of each 1 kpc bin (light pink star symbols in the left panel) from the observed D_{4000} maps (middle panel). The location of R_e is shown as a vertical line in the left panel and as an ellipse in the middle and right panels. The boundary of the spiral arm regions is overplotted as dashed lines on the D_{4000} and residual maps. We find negative D_{4000} radial gradients in both galaxies that support an inside-out formation scenario. Both D_{4000} maps and residual maps indicate lower D_{4000} (younger stellar populations) in the spiral arms of SG 1202 and SG 1204.

7), or D_{4000} (right panel of Fig. 9) between the downstream and the upstream. Observed differences in the azimuthal distributions of Hα, $12 + \log(O/H)$, and D_{4000} may arise due to the different stellar timescales for these tracers, which will be further discussed in Section 4.

4 DISCUSSION

In this section, we discuss the impacts of the boundary between downstream and upstream regions on the results of the MAGPI survey. We illustrate the differences among various ISM tracers and stellar population indicators. It reminds us of the importance of selecting an appropriate indicator when testing the density wave theory through observations. We also compare our observational results with the theoretical expectations derived from the density wave theory and the dynamical spiral theory. In the last subsection, we address the effects of gas flows, which can complicate our test of the density wave theory.

Downloaded from https://academic.oup.com/mnras/article/527/2/2991/7339769 by guest on 22 July 2026

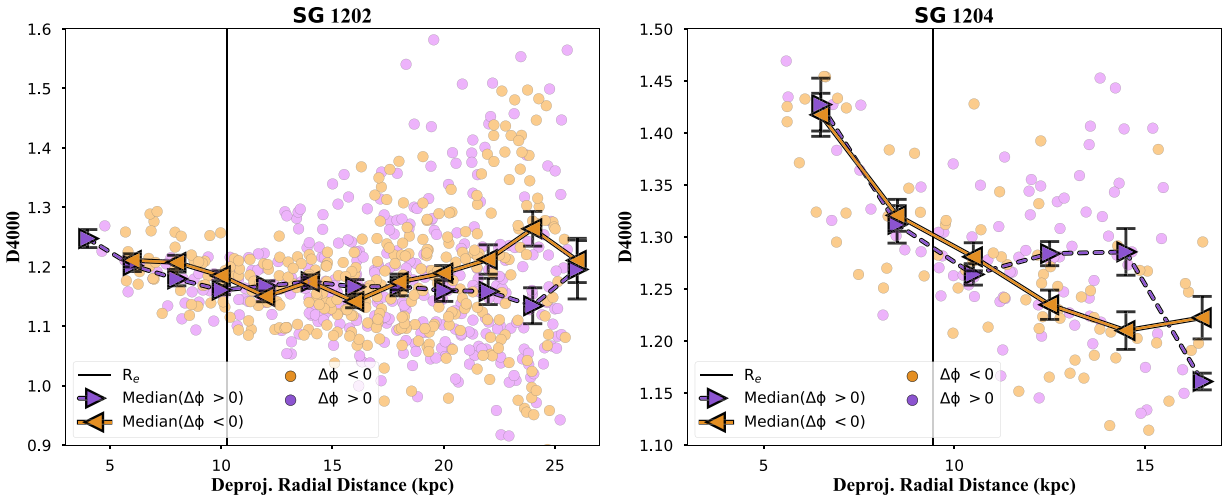

Figure 9. Similar to Fig. 7 but with D_{4000} on the *y*-axis. We find comparable D_{4000} between $\Delta\phi > 0$ (upstream; purple) and $\Delta\phi < 0$ (downstream; orange) in both SG 1202 and SG 1204.

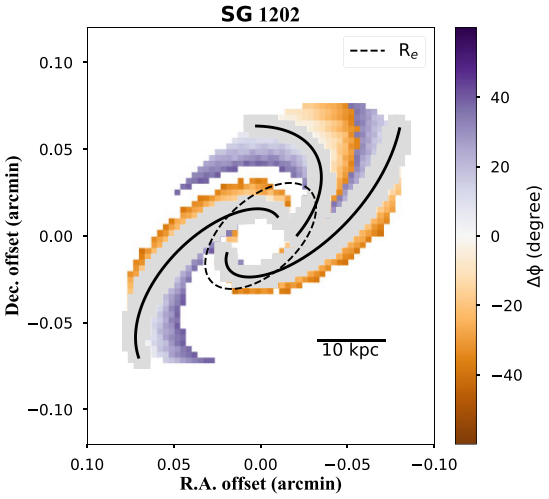

Figure 10. $\Delta\phi$ map after applying the limit of $|\Delta\phi| < 40°$. The grey regions are defined as the spiral arm regions. The limit of the colour bar is matched with Fig. 3 for better comparison.

4.1 Impacts of the boundary between downstream and upstream regions

We find enhanced Σ_{SFR} in the downstream (orange) than the upstream (purple) in SG 1202 but not in D_{4000}. It is important to note that the connection between downstream and upstream at the high $|\Delta\phi|$ end can possibly obscure the signals of offset. To address this, we conduct a test with SG 1202 by employing a $|\Delta\phi|$ limit of $<40°$ (see Fig. 10) and subsequently recompare the downstream and upstream regions. Similarly, we detect a significant azimuthal variation in Σ_{SFR} but not in the 12 + log(O/H) or D_{4000} (Fig. 11). The *p*-value (1.6×10^{-3}) from the KS test suggests the 12 + log(O/H) on both sides of the spiral arms are drawn from different distributions. On the other hand, the *p*-value (7.3×10^{-1}) from the KS test indicates the D_{4000} on both sides of the spiral arms are drawn from the same distribution. These results are consistent with our main findings, where we do not impose a limit on the $|\Delta\phi|$ (see Section 3). Our tests suggest that the linkage between the downstream and the upstream has minimal impact on the azimuthal variation.

4.2 Difference in various tracers

The interpretation of the physics driving our observational trends is impacted by the different time-scales associated with and traced by the ISM and stellar properties. Poggio et al. (2022) find the progressive disappearance of spiral structures in the global metallicity when they gradually include cooler and older stars. Their result hints at the importance of using tracers sensitive to appropriate time-scales when observing spiral structures and material in the interarm regions. We compare and summarize what the different indicators (SFR, gas-phase metallicity, and D_{4000}) trace and their different time-scales in this section.

Only stars more massive than $\sim$20 $M_\odot$ produce a measurable ionizing photon flux. For recently formed stellar populations born through an instantaneous burst, the ionizing photon flux decreases by two orders of magnitude between 5 and 10 Myr after the burst. Thus, the Hα emission is an instantaneous tracer ($\lesssim$30 Myr; Calzetti 2013) of the youngest, most massive, and short-lived rare stars.

Gas-phase metallicity traces metals produced by recent star formation, and it reaches equilibrium within a concise time (a few hundred Myr) compared to the depletion time (Davé, Finlator & Oppenheimer 2011, 2012; Lilly et al. 2013; Sharda et al. 2021). The emission lines we use to measure metallicity are mostly excited by O and B stars, which have formed within the past $\lesssim$10 Myr, and the gas-phase metallicity measured in this way can therefore be treated as the current 'instantaneous' metallicity of the gas out of which the stars have formed.

The D_{4000} is tracing the stellar population ages, while Hα and gas-phase metallicity are indicators for gas ISM properties. The drop in intensity at the blue end of the spectrum is a result of (1) a relative lack of young, bright, blue stars in old stellar populations that dominate the light of a galaxy and (2) increased metal absorption in stellar atmospheres of old and metal-rich stellar populations. D_{4000} is sensitive to starbursts in the past 1–2 Gyr (Kauffmann et al. 2003a), which is tracing a time-scale significantly longer than that of Hα emission and gas-phase metallicity. The long time-scale may allow the latest generation of stars to travel across the disc and reach the next spiral pattern. Because of their rarity and short-lived nature, the massive stars make up a small portion of all stars in a galaxy and thus have a small effect on the mean D_{4000} in the IFS data as opposed to low-mass, cooler, and longer lived stars. Therefore, the influence of

Downloaded from https://academic.oup.com/mnras/article/527/2/2991/7339769 by guest on 22 July 2026

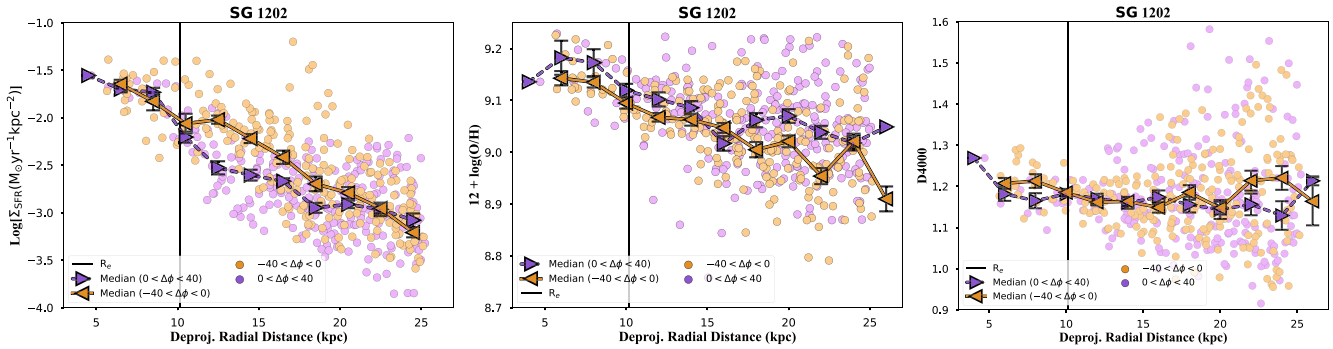

Figure 11. Radial profiles of $\Sigma_{\rm SFR}$, $12 + \log({\rm O/H})$, and D_{4000}, colour coded by the downstream (orange) and upstream (purple). Only spaxels where $|\Delta\phi| < 40^{\circ}$ are considered.

spiral structures on D_{4000} is less significant, compared to Hα as an emission line feature.

We estimate the upper limit of crossing time (t) between two spiral arms by assuming the spiral arms have an equal distance to each other at a radius of $2R_{\rm e}$, using the following equations:

$$D_{\rm arm} = \frac{4\pi R_{\rm e}}{3}, \tag{8}$$

where $D_{\rm arm}$ is simply the circumference at $2R_{\rm e}$ divided by 3 (for a three spiral-arm galaxy),

$$t = \frac{D_{\rm arm}}{v_{\rm rot}}. \tag{9}$$

We adopt the gas rotational velocity ($v_{\rm rot}$) from Sharma et al. (in preparation), which yields the beam-smearing corrected rotational curve based on their 3D modelling method of the ionized gas kinematics. They find that $v_{\rm rot}$ at $2R_{\rm e}$ is 225 and 305 km s^{-1} in SG 1202 and SG 1204, respectively. The galactocentric distance of $2R_{\rm e}$ is 20 kpc for SG 1202 and 18 kpc for SG 1204. The estimated crossing time of SG 1202 (SG 1204) is ∼0.18 Gyr (∼0.12 Gyr), which is shorter than the time-scale to which D_{4000} is sensitive (1–2 Gyr). Thus the absent azimuthal variation in the D_{4000} of SG 1202 and SG 1204 is not unreasonable. Both estimated crossing times are longer than the time-scale to which Hα is sensitive (i.e. $\lesssim$30 Myr). Therefore, the observed azimuthal variation in Hα of SG 1202 is reasonable.

Our work reveals the underlying differences in time-scales traced by gas ISM properties (Hα and gas-phase metallicity) and stellar populations (D_{4000}). When investigating the mechanisms driving spiral features, selecting an indicator sensitive to a time-scale shorter than the crossing time t is crucial. Our pilot sample suggests that an instantaneous or short time-scale tracer (e.g. SFR and gas-phase metallicity) is better suited for testing the density wave theory, compared to D_{4000}.

4.3 Testing the density wave theory

Recently, there have been a growing number of observational tests on the density wave theory and dynamic spiral theory, which are mostly regarding the pattern speed of spiral arms and the differentiation of gas and stellar motion. Because of the challenges in measuring the pattern speed, an indirect method to constrain the origin of spiral features is to determine the location of spiral shocks. The density wave theory expects an offset between the spiral shocks and the spiral pattern while there is no observable offset expected by the dynamic spirals. In SG 1202, we find significantly higher (∼0.25 dex) $\Sigma_{\rm SFR}$ in the leading edge of the spiral arms (downstream; orange). The azimuthal variation in $\Sigma_{\rm SFR}$ suggests that the origin and development of the spiral arms in SG 1202 can be explained by the density wave theory.

Based on the density wave theory, Edmunds (1990) and Ho et al. (2017) construct chemical evolution models that predict an azimuthal variation in the gas-phase metallicity. NGC 1365 (Ho et al. 2017) is observed to show azimuthal variation in the gas-phase metallicity that is consistent with the enhancement effects of spiral arms when material flows across the density waves. However, there are some nearby spiral galaxies showing no azimuthal variation in metallicity (Kreckel et al. 2019).

In this work, we do not observe a significant azimuthal variation in metallicity in SG 1202, unlike NGC 1365 (∼0.2 dex; Ho et al. 2017). The KS test (Section 3.6) shows that the gas-phase metallicities in the downstream and upstream regions of SG 1202 are drawn from different distributions, which is consistent with the chemical evolution models based on the density wave theory.

Dobbs & Pringle (2010) suggest an indirect method to examine the density wave theory through the observed age distribution of stellar clusters. Based on the density wave theory (Lin & Shu 1964), star formation occurs when the gas is compressed and shocked as it periodically passes through the spiral density wave. Because of the differential rotation between material and density wave, the newborn stars move out of the spiral pattern, where the stellar populations inside the corotation radius overtake the spirals, while the stellar populations outside the corotation radius are left behind. This is observable as a red spiral arm with an older stellar population that shows a smaller pitch angle than a blue spiral arm with young stellar ages (Martínez-García, González-López lira & Bruzual-A 2009; Pour-Imani et al. 2016). The density wave theory would thus be observable through an offset between different cluster ages azimuthally across the spiral, whereas dynamic spirals predict no age pattern as material falls into the minimal potential from both sides of the spiral arms, resulting in stars at similar ages lying on both sides of the spirals. This method is widely applied to spatially resolved data (Martínez-García, González-López lira & Bruzual-A 2009; Sánchez-Gil et al. 2011; Shabani et al. 2018; Abdeen et al. 2022), supporting the density wave theory. On the other hand, there are studies that show no age pattern (Choi et al. 2015; Shabani et al. 2018), in agreement with dynamic spirals.

The limited SNR of the continuum in the MAGPI data hinders our ability to determine reliable and resolved stellar ages through SED fitting. In this study, we employ D_{4000} as a stellar age proxy with the necessary spatial resolution. In both SG 1202 and SG 1204, we do not find a statistically significant offset of D_{4000} between the downstream and upstream regions. As detailed in Section 4.2, D_{4000}

Downloaded from https://academic.oup.com/mnras/article/527/2/2991/7339769 by guest on 22 July 2026

is not an ideal indicator for testing the density wave theory due to its long time-scale (1–2 Gyr). Thus, it remains inconclusive to compare the observations and theories regarding stellar ages in the context of density wave theory in this work.

Some of our observations provide evidence that challenges the validity of the density wave theory. In SG 1204, we observe no azimuthal variation in either $\Sigma_{\rm SFR}$ or gas-phase metallicity, which shows a preference for the dynamic spiral theory. It is a caveat that the lack of azimuthal offset results from the combination of (i) more pronounced beam-smearing effects than SG 1202, and (ii) a shorter mixing time-scale in SG 1204, which features tighter pitch angles. We need to expand our study to more MAGPI spiral galaxies to have a better understanding of how pitch angles impact our test of the density wave theory.

4.4 Radial gas flows complicate the comparison between observations and theories

Previous simulations (Di Matteo et al. 2013; Grand et al. 2016; Carr et al. 2022; Orr et al. 2023) have discussed the impact of radial stellar migration and gas flows, induced by asymmetric structures such as spiral arms and stellar bars, on the radial and azimuthal variations of metals. In the Feedback In Realistic Environments 2 (FIRE-2) simulation, Orr et al. (2023) find that the spiral arms act as highways to transfer enriched gas outward, flattening the metallicity radial gradients. The FIRE-2 simulated galaxies show no bias of gas-phase metallicity between the arm and interarm regions when the subgrid turbulent diffusion of metals is considered. Simulations by Khoperskov et al. (2023) reveal that the peak of ISM metal-rich material varies depending on the initial radial ISM metallicity gradient. Specifically, the metal-rich gas is concentrated as a spiral feature in the trailing side of the stellar spiral arm when a radial gradient is present in the simulation. Their simulation does not see large-scale azimuthal variation in metallicity in a spiral galaxy set with no radial gradient. The radial gas flows are important and non-negligible as they potentially impact and complicate the observed metallicity gradient and azimuthal variation. Consequently, they obscure potential observational signatures of density waves and affect our interpretation of the origin of spiral features.

We detect a negative gas-phase metallicity radial gradient in both SG 1202 (-0.069 ± 0.002 dex/$R_{\rm e}$) and SG 1204 (-0.014 ± 0.007 dex/$R_{\rm e}$), consistent with an inside-out galaxy formation. The gradients we measure for these two galaxies are relatively shallow compared to those typically seen in local spiral galaxies in the Calar Alto Legacy Integral Field Area (CALIFA) Survey (-0.1 dex/$R_{\rm e}$; Sánchez et al. 2015), and in the MaNGA survey (-0.14 dex/$R_{\rm e}$; Belfiore et al. 2017). This scenario could be indicative of radial gas flows dispersing and flattening the metal distribution.

The higher gas-phase metallicity observed in the trailing edge of SG 1202 (Fig. 6) is consistent with the simulated galaxy with an initial radial gradient in Khoperskov et al. (2023) The metallicity distribution in SG 1202 could be driven by the density wave theory and/or radial gas flows. In SG 1204, the azimuthal variation of metallicity is non-observable with a flat metallicity radial gradient. This scenario is in line with Khoperskov et al. (2023) where the presence of radial metallicity gradient is essential for azimuthal variation. The dynamic spirals can also result in no azimuthal variation in metallicity. Our current observations are insufficient to discern the dominant physical mechanisms driving the spiral features in SG 1202 and SG 1204.

5 CONCLUSIONS

We study the two-dimensional distributions of $\Sigma_{\rm SFR}$ (Hα), gas-phase metallicity, and D_{4000} in two three-armed spiral galaxies, SG 1202 and SG 1204, at $z \sim 0.3$ (3–4 Gyr ago) from the MAGPI survey (Foster et al. 2021). The goal of our study is to investigate the driving physics of spiral arm formation and how the different physical mechanisms impact and vary the ISM and stellar properties within and upstream/downstream from the spiral arms. Specifically, we compare our findings with the expectations from two spiral arm formation mechanisms: density wave theory and dynamic spirals.

In SG 1202, we observe higher $\Sigma_{\rm SFR}$ (Fig. 4), systematically lower metallicity (Fig. 6), and younger stellar age (Fig. 8) in the spiral arms than the interarms. In SG 1204, we do not find a statistically significant difference in metallicity (Fig. 6) or D_{4000} (Fig. 8) between the arms and interarms. We do, however, recover higher $\Sigma_{\rm SFR}$ (Fig. 4) in the arms of SG 1204. These results support the enhancement of star formation within the arm regions. The diversity in the metallicity and stellar age azimuthal trends between SG 1202 and SG 1204 may be a result of a combination of beam-smearing effects and/or shorter mixing time-scale, likely due to the tighter pitch angles in SG 1204 compared to SG 1202.

We find higher $\Sigma_{\rm SFR}$ in the leading edge of spiral arms ($\Delta\phi < 0$; downstream) in SG 1202 (Fig. 5). This matches the expectation of the density wave theory. The observed higher metallicity in the trailing edge of the spiral arms of SG 1202 (Fig. 7) is consistent with the expectations of radial gas flows driven by spiral arms (Khoperskov et al. 2023). SG 1204, on the other hand, does not show a statistically significant offset in the $\Sigma_{\rm SFR}$ (Fig. 5) or metallicity (Fig. 7) between both sides of the spiral arms. Our findings for SG 1204 are consistent with the dynamic spiral theory. This could also be impacted by radial gas flows, which is consistent with the simulated spiral galaxies with no radial gradients in Khoperskov et al. (2023). We are however unable to determine the dominant mechanism driving the observations based on the current data.

Neither galaxy shows an azimuthal variation in the D_{4000} (Fig. 9), which may be a consequence of the long time-scale (1–2 Gyr) traced by D_{4000}. This reflects the importance of choosing an indicator sensitive to changes in star formation on time-scales shorter than the travel time between two spiral arms.

The effects of spiral arms on the ISM are a complex question requiring further high-resolved observational data across cosmic time. This work is a pilot project with two spiral galaxies at $z \sim 0.3$, with a plan to expand the data to the entire MAGPI survey.

ACKNOWLEDGEMENTS

We thank the anonymous referee for their constructive and detailed comments that improved the quality of this work. We thank Paul Torrey for constructive and enlightening comments and suggestions on this work.

We wish to thank the ESO staff, and in particular the staff at Paranal Observatory, for carrying out the MAGPI observations. MAGPI targets were selected from GAMA. GAMA is a joint European–Australasian project based around a spectroscopic campaign using the Anglo-Australian Telescope. GAMA is funded by the STFC (UK), the ARC (Australia), the AAO, and the participating institutions. GAMA photometry is based on observations made with ESO Telescopes at the La Silla Paranal Observatory under programme IDs 179.A-2004 and 177.A-3016. Parts of this work are supported by the Australian Research Council Centre of Excellence for All Sky Astrophysics in 3 Dimensions (ASTRO 3D), through project number

Downloaded from https://academic.oup.com/mnras/article/527/2/2991/7339769 by guest on 22 July 2026

CE170100013. KG is supported by the Australian Research Council through the Discovery Early Career Researcher Award (DECRA) Fellowship (project number DE220100766) funded by the Australian Government. PS is supported by Leiden University Oort Fellowship and the IAU Gruber Foundation Fellowship. CF is the recipient of an Australian Research Council Future Fellowship (project number FT210100168) funded by the Australian Government. CDPL, JTM, and CF are the recipients of ARC Discovery Project DP210101945. GS thanks SARAO post-doctoral fellowship (grant no. 97882). LMV acknowledges support from the German Academic Scholarship Foundation (Studienstiftung des Deutschen Volkes), the Marianne-Plehn-Program of the Elite Network of Bavaria, and the COMPLEX project from the European Research Council (ERC) under the European Union's Horizon 2020 Framework Programme grant agreement ERC-2019-AdG 882679.

This research has made use of NASA's Astrophysics Data System Bibliographic Services (ADS). This research made use of ASTROPY,[5] a community-developed core PYTHON package for Astronomy (Astropy Collaboration 2013, 2018). This research has made use of the NASA/IPAC Extragalactic Database (NED) that is operated by the Jet Propulsion Laboratory, California Institute of Technology, under contract with NASA. Parts of the results in this work make use of the colour maps in the CMASHER package (van der Velden 2020).

DATA AVAILABILITY

The data used in this paper are available under the MAGPI survey on the ESO public archive (1104.B-0536). The reduced MAGPI MUSE data cubes and emission line data products will be made publicly available in forthcoming papers by Mendel et al. (in preparation) and Battisti et al. (in preparation), respectively. Additional data generated by the analyses in this work are available upon request to the corresponding author.

REFERENCES

Abdeen S. et al., 2022, MNRAS, 512, 366
Aouad C. J., James P. A., Chilingarian I. V., 2020, MNRAS, 496, 5211
Astropy Collaboration, 2013, A&A, 558, A33
Astropy Collaboration, 2018, AJ, 156, 123
Baba J., 2015, MNRAS, 454, 2954
Baba J., Saitoh T. R., Wada K., 2013, ApJ, 763, 46
Baldwin J. A., Phillips M. M., Terlevich R., 1981, PASP, 93, 5
Belfiore F. et al., 2017, MNRAS, 469, 151
Bernardi M., Shankar F., Hyde J. B., Mei S., Marulli F., Sheth R. K., 2010, MNRAS, 404, 2087
Bianco F., Modjaz M., Oh S., Fierroz D., Liu Y., Kewley L., Graur O., 2016, Astron. Comput., 16, 54
Bittner A. et al., 2019, A&A, 628, A117
Bonnell I. A., Dobbs C. L., Robitaille T. P., Pringle J. E., 2006, MNRAS, 365, 37
Brinchmann J., Charlot S., White S. D. M., Tremonti C., Kauffmann G., Heckman T., Brinkmann J., 2004, MNRAS, 351, 1151
Bundy K. et al., 2015, ApJ, 798, 7
Calzetti D., 2013, in Falcón-Barroso J., Knapen J. H., eds, Secular Evolution of Galaxies. Cambridge Univ. Press, Cambridge, p. 419
Cantalupo S. et al., 2019, MNRAS, 483, 5188
Canzian B., 1993, ApJ, 414, 487
Cappellari M., 2017, MNRAS, 466, 798
Cappellari M., Copin Y., 2012, Astrophysics Source Code Library, record ascl:1211.006
Cappellari M., Emsellem E., 2004, PASP, 116, 138
Carr C., Johnston K. V., Laporte C. F. P., Ness M. K., 2022, MNRAS, 516, 5067
Chabrier G., 2003, PASP, 115, 763
Chen Q.-H., Grasha K., Battisti A. J., Kewley L. J., Madore B. F., Seibert M., Rich J. A., Beaton R. L., 2023, MNRAS, 519, 4801
Choi Y., Dalcanton J. J., Williams B. F., Weisz D. R., Skillman E. D., Fouesneau M., Dolphin A. E., 2015, ApJ, 810, 9
Crain R. A. et al., 2015, MNRAS, 450, 1937
Croom S. M. et al., 2021, MNRAS, 505, 991
Davé R., Finlator K., Oppenheimer B. D., 2011, MNRAS, 416, 1354
Davé R., Finlator K., Oppenheimer B. D., 2012, MNRAS, 421, 98
Davis D. R., Hayes W. B., 2014, ApJ, 790, 87
Di Matteo P., Haywood M., Combes F., Semelin B., Snaith O. N., 2013, A&A, 553, A102
Dobbs C., Baba J., 2014, Publ. Astron. Soc. Aust., 31, e035
Dobbs C. L., Bonnell I. A., 2008, MNRAS, 385, 1893
Dobbs C. L., Pringle J. E., 2010, MNRAS, 409, 396
D'Onghia E., Vogelsberger M., Hernquist L., 2013, ApJ, 766, 34
Edmunds M. G., 1990, MNRAS, 246, 678
Egusa F., Sofue Y., Nakanishi H., 2004, PASJ, 56, L45
Egusa F., Kohno K., Sofue Y., Nakanishi H., Komugi S., 2009, ApJ, 697, 1870
Elmegreen B. G., Elmegreen D. M., Seiden P. E., 1989, ApJ, 343, 602
Falcón-Barroso J. et al., 2006, MNRAS, 369, 529
Fitzpatrick E. L., Massa D., Gordon K. D., Bohlin R., Clayton G. C., 2019, ApJ, 886, 108
Foster C. et al., 2021, Publ. Astron. Soc. Aust., 38, e031
Foyle K., Rix H. W., Dobbs C. L., Leroy A. K., Walter F., 2011, ApJ, 735, 101
Fuchs B., 2001, A&A, 368, 107
Fujii M. S., Baba J., Saitoh T. R., Makino J., Kokubo E., Wada K., 2011, ApJ, 730, 109
Garcia A. M. et al., 2023, MNRAS, 519, 4716
Ghosh S., Jog C. J., 2016, MNRAS, 459, 4057
Goldreich P., Lynden-Bell D., 1965, MNRAS, 130, 125
Grand R. J. J., Kawata D., Cropper M., 2012a, MNRAS, 421, 1529
Grand R. J. J., Kawata D., Cropper M., 2012b, MNRAS, 426, 167
Grand R. J. J. et al., 2016, MNRAS, 460, L94
Grasha K. et al., 2017, ApJ, 842, 25
Grasha K. et al., 2022, ApJ, 929, 118
Ho I. T. et al., 2017, ApJ, 846, 39
Hockney R. W., Brownrigg D. R. K., 1974, MNRAS, 167, 351
Hohl F., 1971, ApJ, 168, 343
Jin Y., Kewley L. J., Sutherland R. S., 2022, ApJ, 934, L8
Kauffmann G. et al., 2003a, MNRAS, 341, 33
Kauffmann G. et al., 2003b, MNRAS, 346, 1055
Kennicutt R. C. J., 1998, ARA&A, 36, 189
Kewley L. J., Dopita M. A., 2002, ApJS, 142, 35
Kewley L. J., Dopita M. A., Sutherland R. S., Heisler C. A., Trevena J., 2001, ApJ, 556, 121
Kewley L. J., Rupke D., Zahid H. J., Geller M. J., Barton E. J., 2010, ApJ, 721, L48
Kewley L. J., Nicholls D. C., Sutherland R. S., 2019, ARA&A, 57, 511
Khoperskov S., Sivkova E., Saburova A., Vasiliev E., Shustov B., Minchev I., Walcher C. J., 2023, A&A, 671, A56
Kreckel K. et al., 2019, ApJ, 887, 80
Law D. R., Shapley A. E., Steidel C. C., Reddy N. A., Christensen C. R., Erb D. K., 2012, Nature, 487, 338
Lazariv T., Lehmann C., 2018, preprint (arXiv:1810.09753)
Li Z., Krumholz M. R., Wisnioski E., Mendel J. T., Kewley L. J., Sánchez S. F., Galbany L., 2021, MNRAS, 504, 5496
Lilly S. J., Carollo C. M., Pipino A., Renzini A., Peng Y., 2013, ApJ, 772, 119
Lin C. C., Shu F. H., 1964, ApJ, 140, 646
Lin C. C., Shu F. H., 1966, Proc. Natl. Acad. Sci., 55, 229
Lindblad P. A. B., Lindblad P. O., Athanassoula E., 1996, A&A, 313, 65
Lintott C. J. et al., 2008, MNRAS, 389, 1179

[5]http://www.astropy.org

Downloaded from https://academic.oup.com/mnras/article/527/2/2991/7339769 by guest on 22 July 2026

Lintott C. et al., 2011, MNRAS, 410, 166
Maiolino R., Mannucci F., 2019, A&AR, 27, 3
Margalef-Bentabol B., Conselice C. J., Haeussler B., Casteels K., Lintott C., Masters K., Simmons B., 2022, MNRAS, 511, 1502
Marino R. A. et al., 2012, ApJ, 754, 61
Martig M., Bournaud F., Croton D. J., Dekel A., Teyssier R., 2012, ApJ, 756, 26
Martínez-García E. E., González-López lira R. A., Bruzual-A G., 2009, ApJ, 694, 512
Michikoshi S., Kokubo E., 2016, ApJ, 821, 35
Miller R. H., Prendergast K. H., Quirk W. J., 1970, ApJ, 161, 903
Noll S., Burgarella D., Giovannoli E., Buat V., Marcillac D., Muñoz-Mateos J. C., 2009, A&A, 507, 1793
Oh S. H., Kim W.-T., Lee H. M., Kim J., 2008, ApJ, 683, 94
Orr M. E. et al., 2023, MNRAS, 521, 3708
Perez J., Michel-Dansac L., Tissera P. B., 2011, MNRAS, 417, 580
Peterken T. G., Merrifield M. R., Aragón-Salamanca A., Drory N., Krawczyk C. M., Masters K. L., Weijmans A.-M., Westfall K. B., 2019, Nat. Astron., 3, 178
Pettitt A. R., Tasker E. J., Wadsley J. W., Keller B. W., Benincasa S. M., 2017, MNRAS, 468, 4189
Pettitt A. R., Dobbs C. L., Baba J., Colombo D., Duarte-Cabral A., Egusa F., Habe A., 2020, MNRAS, 498, 1159
Poggio E. et al., 2022, A&A, 666, L4
Pour-Imani H., Kennefick D., Kennefick J., Davis B. L., Shields D. W., Shameer Abdeen M., 2016, ApJ, 827, L2
Ramón-Fox F. G., Bonnell I. A., 2022, MNRAS, 512, 1111
Reid M. J. et al., 2014, ApJ, 783, 130
Roberts W. W., Jr, 1970, in Becker W., Kontopoulos G. I., eds, Proc. IAU Symp. 38, The Spiral Structure of our Galaxy. Reidel, Dordrecht, p. 415
Robotham A. S. G. et al., 2011, MNRAS, 416, 2640
Robotham A. S. G., Davies L. J. M., Driver S. P., Koushan S., Taranu D. S., Casura S., Liske J., 2018, MNRAS, 476, 3137
Rodríguez-Baras M., Díaz A. I., Rosales-Ortega F. F., Sánchez S. F., 2018, A&A, 609, A102
Rosario D. J., Mendel J. T., Ellison S. L., Lutz D., Trump J. R., 2016, MNRAS, 457, 2703
Rupke D. S. N., Kewley L. J., Barnes J. E., 2010a, ApJ, 710, L156
Rupke D. S. N., Kewley L. J., Chien L. H., 2010b, ApJ, 723, 1255
Salpeter E. E., 1955, ApJ, 121, 161
Sánchez S. et al., 2015, Galaxies, 3, 164
Sánchez-Gil M. C., Jones D. H., Pérez E., Bland-Hawthorn J., Alfaro E. J., O'Byrne J., 2011, MNRAS, 415, 753
Sánchez-Menguiano L. et al., 2018, A&A, 609, A119
Sarzi M. et al., 2006, MNRAS, 366, 1151
Sellwood J. A., 2011, MNRAS, 410, 1637
Sellwood J. A., Carlberg R. G., 1984, ApJ, 282, 61
Sellwood J. A., Carlberg R. G., 2014, ApJ, 785, 137
Sellwood J. A., Carlberg R. G., 2019, MNRAS, 489, 116
Sellwood J. A., Masters K. L., 2022, ARA&A, 60, 36
Sempere M. J., Garcia-Burillo S., Combes F., Knapen J. H., 1995, A&A, 296, 45
Shabani F. et al., 2018, MNRAS, 478, 3590
Sharda P., Krumholz M. R., Wisnioski E., Forbes J. C., Federrath C., Acharyya A., 2021, MNRAS, 502, 5935
Sharda P., Ginzburg O., Krumholz M. R., Forbes J. C., Wisnioski E., Mingozzi M., Zovaro H. R. M., Dekel A., 2023, preprint (arXiv:2303.15853)
Soto K. T., Lilly S. J., Bacon R., Richard J., Conseil S., 2016, MNRAS, 458, 3210
Struck C., Dobbs C. L., Hwang J.-S., 2011, MNRAS, 414, 2498
Tamburro D., Rix H. W., Walter F., Brinks E., de Blok W. J. G., Kennicutt R. C., Mac Low M. M., 2008, AJ, 136, 2872
Taylor E. N. et al., 2011, MNRAS, 418, 1587
Thomasson M., Elmegreen B. G., Donner K. J., Sundelius B., 1990, ApJ, 356, L9
Toomre A., 1977, ARA&A, 15, 437
van der Velden E., 2020, J. Open Source Softw., 5, 2004
Vollmer B., Wong O. I., Braine J., Chung A., Kenney J. D. P., 2012, A&A, 543, A33
Wada K., Baba J., Saitoh T. R., 2011, ApJ, 735, 1
Weilbacher P. M. et al., 2020, A&A, 641, A28
Wild V., Charlot S., Brinchmann J., Heckman T., Vince O., Pacifici C., Chevallard J., 2011, MNRAS, 417, 1760
Willett K. W. et al., 2013, MNRAS, 435, 2835
Wisnioski E. et al., 2015, ApJ, 799, 209
Zhang K. et al., 2017, MNRAS, 466, 3217

APPENDIX: IDENTIFIED SPIRAL ARMS FROM SPARCFIRE

In Section 3.3, we introduce our method of defining the spiral arm ridge lines. The initially defined spiral arms from SPARCFIRE are overplotted on the deprojected white-light images of our galaxies in the left column of Fig. A1. We fine-tune the starting and ending radii of the spiral ridge lines to improve their alignment with the observed white-light images, shown in the right column of Fig. A1. The red spiral arms are clockwise with positive pitch angles, while the blue ones are counterclockwise with negative pitch angles.

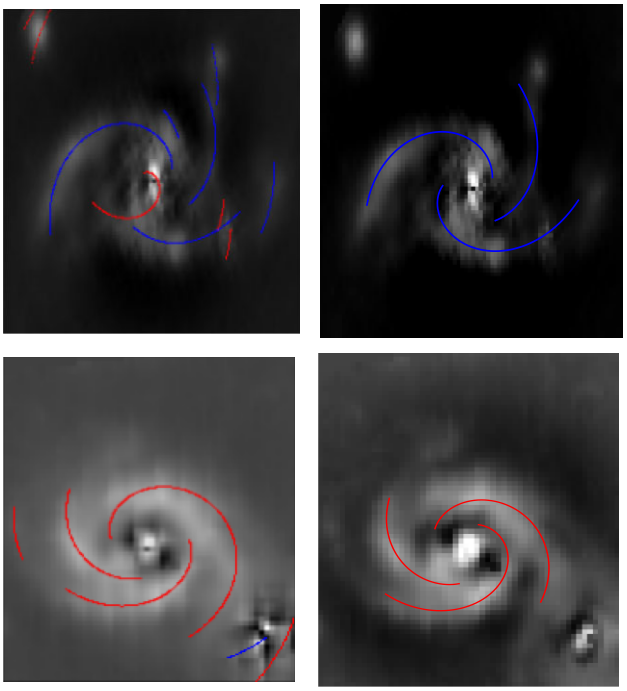

Figure A1. Left column: the spiral arm ridge initially defined by SPARCFIRE, overplotted on the deprojected white-light images after subtracted by the Sérsic profile. The red spiral arms are clockwise, while the blue ones are counterclockwise. Right column: the final accepted spiral arm ridge after we fine-tune the starting and ending radii of the spiral arms to improve their alignment with the observed white-light images. The top panels show the SG 1202, while the bottom panels show the SG 1204.

This paper has been typeset from a TEX/LATEX file prepared by the author.

Downloaded from https://academic.oup.com/mnras/article/527/2/2991/7339769 by guest on 22 July 2026

© The Author(s) 2023.
Published by Oxford University Press on behalf of Royal Astronomical Society. This is an Open Access article distributed under the terms of the Creative Commons Attribution License (http://creativecommons.org/licenses/by/4.0/), which permits unrestricted reuse, distribution, and reproduction in any medium, provided the original work is properly cited.